Altitude-Dependent Role of Nitric Acid in Iodic Acid-Iodous Acid Nucleation: From Marine Boundary Layer Catalyst to Upper Troposphere Core Component

Jiaze Zhang[1], Ling Liu[1], An Ning[1], Haotian Zu[1], Jing Li[1], Fengyang Bai[1,2], Jie Yang[1], Xueshun Chen[3], and Xiuhui Zhang[1]

[1] State Key Laboratory of Environment Characteristics and Effects for Near-space, Beijing Key Laboratory of Intelligent Molecular Materials and High-throughput Manufacturing, Key Laboratory of Cluster Science, Ministry of Education of China, School of Chemistry and Chemical Engineering, Beijing Institute of Technology, Beijing, 100081, China.
[2] Institute of Catalysis for Energy and Environment, College of Chemistry and Chemical Engineering, Shenyang Normal University, Shenyang, 110034, China.
[3] The State Key Laboratory of Atmospheric Boundary Layer Physics and Atmospheric Chemistry, Institute of Atmospheric Physics, Chinese Academy of Sciences, Beijing, 100029, China

Correspondence to: Ling Liu (lingliu@bit.edu.cn), and Xiuhui Zhang (zhangxiuhui@bit.edu.cn)

Abstract. With global sulfur emissions declining and concurrent marine iodine emissions rising, new particle formation (NPF) driven by iodic acid (HIO_3) and iodous acid (HIO_2) has become critical to global aerosol and cloud condensation nuclei (CCN) budget. However, the role of ubiquitous nitric acid (HNO_3) in this iodine-driven nucleation across altitudes from the marine boundary layer (MBL) to the upper troposphere (UT) remains poorly understood. Here, we integrated quantum chemical calculations with Atmospheric Cluster Dynamics Code (ACDC) simulations to unravel the altitude-dependent enhancement mechanism by which HNO_3 enhances HIO_3–HIO_2 nucleation. Under MBL conditions, HNO_3 acts as a catalyst to promote nucleation via collision and re-evaporation processes, yielding a modest 2-3-fold enhancement in nucleation. In contrast, as altitude increases to the UT, where cluster evaporation is effectively suppressed by low temperature, HNO_3 becomes a core component of nucleation clusters, driving a 200-fold enhancement on the cluster formation rate. Consequently, the simulated cluster formation rates of the HNO_3–HIO_3–HIO_2 mechanism reach 10^3–10^4 cm^{-3} s^{-1}, exceeding those of the well-documented H_2SO_4–NH_3–HNO_3 mechanism under comparable UT conditions. Our findings establish HNO_3 as a critical atmospheric agent that amplifies iodine oxoacid nucleation across altitudes, providing a critical chemical explanation for intense NPF events in both polluted coastal regions and the UT. This altitude-dependent role of HNO_3 links marine iodine emissions to troposphere-wide particle formation, with important implications for global CCN budgets and the refinement of climate models.

1 Introduction

Atmospheric aerosols exert critical impacts on air quality, human health, and global climate change (Haywood and Boucher, 2000; Pope and Dockery, 2006; Fan et al., 2016; Hirshorn et al., 2022), primarily by acting as cloud condensation nuclei (CCN) that modulate cloud microphysics (Fan et al., 2016; Li et al., 2022). New particle formation (NPF) accounts for ~ 50% of

global CCN (Kulmala et al., 2013; Williamson et al., 2019) and is the dominant particle source in the upper troposphere (UT) (Gordon et al., 2017), thus serving as a key process linking atmospheric chemistry to climate regulation. Nucleation is recognized as the key step in NPF processes (Zhang, 2010; Kulmala et al., 2013). Due to the chemical complexity of nucleation precursors and the sensitivities to ambient conditions, identifying molecular-level mechanisms during the critical nucleation stage remains a persistent challenge in atmospheric chemistry (Zhang et al., 2012).

Conventional sulfuric acid (H_2SO_4)-dominated nucleation mechanisms fail to account for the observed concentrations of particulate matter in the boundary layer and cloud condensation nuclei in the upper troposphere (Williamson et al., 2019). With declining global sulfur emissions (Aas et al., 2019) and rising marine iodine emissions (Cuevas et al., 2018; Legrand et al., 2018), recent studies have identified marine-derived iodine oxoacids, iodic acid (HIO_3) (Sipilä et al., 2016) and iodous acid (HIO_2) (He et al., 2021), as important nucleation precursors in marine (Liu et al., 2023; Bai et al., 2025), polar (Baccarini et al., 2020; He et al., 2021; Li et al., 2024a), and even high-altitude environments (Koenig et al., 2020; Salignat et al., 2024; Li et al., 2024a). Studies show that HIO_3 and HIO_2 can form stable clusters via acid–base interactions and halogen bonds (Liu et al., 2023; Ma et al., 2023). However, this binary HIO_3–HIO_2 nucleation mechanism alone cannot explain the intense NPF events observed in polluted coastal regions (e.g., Zhejiang, China), suggesting that additional atmospheric species may participate in and promote iodine oxoacid-driven nucleation processes (Yu et al., 2019; Ma et al., 2023), yet these species remain unidentified and uncharacterized.

Nitric acid (HNO_3) is one of the most widespread and abundant inorganic acids in the atmosphere, present throughout the marine boundary layer (MBL) and upper troposphere (UT), with sources including anthropogenic emissions (Wang et al., 2021) and natural processes such as lightning (Tost, 2017). Previous studies have confirmed that HNO_3 stabilizes atmospheric molecular clusters via hydrogen bonds and proton-transfer driven electrostatic interactions in both H_2SO_4–dimethylamine (DMA) (Liu et al., 2021) and H_2SO_4–NH_3 (Liu et al., 2018; Wang et al., 2022) nucleation systems, and since iodine oxoacids readily form hydrogen- and halogen-bond networks, the ubiquitous and co-located HNO_3 is a strong candidate for the additional species that promotes iodine-driven nucleation (Zhang et al., 2023; Zu et al., 2023, 2024). Importantly, HNO_3 and iodine precursors extensively coexist across altitudes. Specifically, nitrate and iodate are simultaneously detected in the free troposphere (FT) (Frege et al., 2017), and both iodine species (Koenig et al., 2020) and HNO_3 are observed in the UT (Jurkat et al., 2014). However, nitrate-based chemical ionization, commonly used for neutral cluster detection, tends to mask HNO_3's involvement in iodine-driven nucleation (Sipilä et al., 2016), leaving its molecular mechanism and environmental dependence unclear.

Notably, atmospheric temperature, condensation sink, and precursor concentrations vary sharply with altitude, giving rise to strong altitude-dependent behavior in atmospheric nucleation. To date, no study has revealed how HNO_3 regulates iodine oxoacid nucleation from the MBL to the UT. Consequently, fundamental questions remain unanswered: Can HNO_3 interact with HIO_3 and HIO_2 to form critical nucleation clusters? What is the molecular mechanism by which HNO_3 interacts with HIO_3–HIO_2 clusters? How does the role of HNO_3 in HIO_3–HIO_2 nucleation shift with altitude from the MBL to the UT?

Answering these questions will help us elucidate how marine iodine emissions shape troposphere-wide NPF and the global CCN budget under the sulfur emission reduction.

Here, we combine high-level quantum chemical calculations and Atmospheric Cluster Dynamics Code (ACDC) (McGrath et al., 2012) simulations to systematically unravel the altitude-dependent mechanism of the role of HNO_3 in HIO_3–HIO_2 nucleation. We reveal the molecular nature of iodine-containing cluster stabilization by HNO_3, quantify nucleation rates and pathway evolution along the vertical atmospheric profile, and evaluate the new mechanism against classic nucleation schemes. Our results establish the functional transition of HNO_3 from a catalyst in the MBL to a core cluster component in the UT, providing critical theoretical support for interpreting global iodine-driven NPF and improving aerosol representations in climate models.

2 Methods

2.1 Configurational sampling workflow

This study employed a multi-step computational workflow to optimize configurations and calculate energies for $(HNO_3)_x(HIO_3)_y(HIO_2)_z$ clusters ($2 \le x + y + z \le 6$, $1 \le x \le 3$). The constraint of $1 \le x \le 3$ is applied because HNO_3 exhibits a relatively weak self-binding ability (Liu et al., 2021; Zu et al., 2023), requiring the participation of HIO_2 to form stable clusters. The initial structures of $(HIO_3)_y(HIO_2)_z$ ($2 \le y + z \le 6$) clusters were adopted from our previous study (Liu et al., 2023; Zu et al., 2024). Initially, the ABCluster program (Zhang and Dolg, 2015) with the UFF force field (Rappe et al., 1992) was employed to systematically generate initial configurations, yielding 5,000 low-energy candidate structures for each cluster. Given the inability of the Universal Force Field (UFF) to describe proton transfer, ions in distinct protonation states were utilized to model hydrogen bonding and proton transfer (Kubečka et al., 2019). The ionic species considered include IO_3^-, NO_3^- and the protonated counterpart $H_2IO_2^+$. These structures were then subjected to preliminary optimization with the PM7 (Stewart, 2013) semi-empirical method in MOPAC2016 program (Stewart, 2016) to filter for 100 low-energy configurations. Despite exhaustive sampling within the computational budget, selecting the lowest 100 configurations based on PM7 calculations may still result in the true global minimum being missed (Kurfman et al., 2021). In addition, we manually constructed a set of candidate structures with multiple hydrogen- and halogen-bonding structures based on chemical intuition. All subsequent Density Functional Theory (DFT) optimizations were performed with the Gaussian 09 package, consistently using the ωB97X-D functional and a FineGrid for integration, which has been benchmarked and widely adopted for describing noncovalent interactions in atmospheric molecular clusters (Elm et al., 2013). This DFT stage proceeded in two steps with different basis sets. First, the 100 most stable configurations were reoptimized using the 6-31+G* (for H, O, and N) + Lanl2DZ (for I) basis sets (Elm and Kristensen, 2017). Subsequently, a final high-precision reoptimization with tight convergence criteria was performed on the 10 most stable isomers. To ensure accuracy for atmospheric systems, the 6-311++G(3df,3pd) basis set was assigned to H, O, and N, in combination with the aug-cc-pVTZ-PP basis set and ECP28MDF for I (Francl et al., 1982; Peterson et al., 2003). As demonstrated by previous benchmark studies, this combination provides highly reliable estimates of binding

energies (Elm et al., 2012, 2013). Vibrational frequency calculations were performed at this final level to confirm the optimized structures were true energy minima.

2.2 Quantum Chemistry Calculation

The Gibbs free energies (ΔG, kcal mol^{-1}) of the optimized clusters at a reference pressure of 1 atm were calculated using the following equation:

$$\Delta G = \Delta E_{\text{DLPNO-CCSD(T)}} + \Delta E_{\text{SOC}} + \Delta G_{\text{thermal}}^{\omega\text{B97X-D}} \quad (1)$$

The terms in eq 1 were derived as follows: (1) The electronic energy term ($\Delta E_{\text{DLPNO-CCSD(T)}}$), intended to refine binding energies with high accuracy, was obtained from the single point calculations using ORCA 5.0 program (Neese, 2012) at the DLPNO-CCSD(T)/aug-cc-pVTZ (for H, O, and N) + aug-cc-pVTZ-PP with ECP28MDF (for I) level of theory with TightPNO and TightSCF settings. (2) Spin-orbit coupling (SOC) effects play a significant role in the thermodynamic properties of atmospheric iodine species due to their heavy-atom nature, as previously demonstrated by foundational studies (Khanniche et al., 2016, 2017; Engsvang et al., 2024). In this study, the SOC correction (ΔE_{SOC}) was evaluated by computing the energy difference between calculations performed with and without SOC potential. These calculations were performed using Gaussian 16 (Frisch et al., 2016) at the ωB97X-D/6-311++G(3df,3pd) (for H, N and O) + dhfTZVP-2c (for I) level of theory (Chan and Yim, 2013; Kühn and Weigend, 2015; Sarr et al., 2021; Holzer et al., 2022). (3) Temperature-dependent free energy corrections ($\Delta G_{\text{thermal}}^{\omega\text{B97X-D}}$) were computed at the ωB97X-D/6-311++G(3df,3pd) (for H, O, and N) + aug-cc-pVTZ-PP with ECP28MDF (for I) level. The Shermo 2.6 code (Lu and Chen, 2021) was used to calculate free energy values at specified atmospheric temperatures (204-288 K). The ΔG of the optimized clusters at various temperatures are summarized in Table S1.

2.3 Wave Function Analysis

The wavefunction from quantum calculations was analyzed using Multiwfn 3.7 (Lu and Chen, 2012) with results visualized via VMD software (Humphrey et al., 1996), to investigate the intermolecular interactions responsible for the identified cluster conformations. Potential binding sites were identified by mapping the electrostatic potential (ESP) onto the Van der Waals (vdW) surface, defined by the 0.001 a.u. electron density contour, to distinguish electron-rich (electronegative) and electron-deficient (electropositive) regions prone to noncovalent bonding. For quantitative evaluation of interaction strengths, the Atoms in Molecules (AIM) theory (Lane et al., 2013) was employed to calculate key topological properties at bond critical points (BCPs), including electron density $\rho(r)$, Laplacian of electron density $\nabla^2\rho(r)$, and local energy density $H(r)$, as shown in Table S2.

2.4 Atmospheric cluster dynamics code (ACDC) simulation

To quantitatively investigate nucleation kinetics, including cluster formation rates and growth pathways, the ACDC (McGrath et al., 2012) was employed to numerically solve the birth-death equations (Eq. 2). These equations describe the temporal evolution of cluster concentrations by integrating collision, evaporation, source, and sink processes:

$$\frac{\mathrm{d}c_i}{\mathrm{d}t} = \frac{1}{2}\sum_{j<i}\beta_{j,(i-j)}c_j c_{(i-j)} + \sum_j \gamma_{(i+j)\to i}c_{i+j} - \sum_j \beta_{i,j}c_i c_j - \frac{1}{2}\sum_{j<i}\gamma_{i\to j}c_i + Q_i - S_i \quad (2)$$

where c_i denotes the concentration of cluster i, $\beta_{j,(i-j)}$ represents the collision rate coefficient between clusters j and (i - j), and $\gamma_{(i+j)\to i}$ corresponds to the evaporation rate coefficient for cluster (i + j) dissociating into clusters i and j. External sources and size-dependent sinks are quantified by Q_i and S_i, respectively. Details for calculating $\beta_{j,(i-j)}$ and $\gamma_{(i+j)\to i}$ are presented in the Supporting Information. In the ACDC simulations, kinetically stable clusters are characterized as those capable of continuous growth rather than dissociation via evaporation, as quantified by the criterion $\beta c/\sum\gamma > 1$. Correspondingly, the boundary conditions are set as seven-molecule clusters, representing the smallest kinetically stable clusters that grow beyond the six-molecule simulation system. Boundary clusters were determined individually for each ACDC simulation: temperature-dependent β and $\sum\gamma$ coefficients were first calculated for each cluster, and those satisfying the criterion $\beta c/\sum\gamma > 1$ at the given monomer concentration (c) were defined as boundary clusters. Here, the c denotes the gas-phase concentration of the actual colliding species (HNO_3, HIO_3, or HIO_2). Representative boundary conditions under various temperature and concentration scenarios are provided in Table S3.

To account for intermolecular vdW force enhancement, a factor of 2.3 was applied to $\beta_{i,j}$, consistent with prior simulations (Halonen et al., 2019). Additionally, a size-dependent sink term (Lehtipalo et al., 2016) S_i is used to quantify cluster losses:

$$S_i = \mathrm{CS}_{\mathrm{ref}} \times \left(d_i / d_{\mathrm{ref}}\right)^{-m} \quad (3)$$

where d_i is the diameter of cluster i, $\mathrm{CS}_{\mathrm{ref}}$ is the condensation sink for a reference monomer, and m is set to 1.7, which depends on scavenger distributions and is consistent with typical atmospheric aerosols (Lehtinen et al., 2007).

3 Results and Discussion

3.1 Molecular Interactions

The formation of thermodynamically stable atmospheric clusters is governed by intermolecular interactions between nucleation precursors, primarily hydrogen bonds (HB) and halogen bonds (XB). To identify potential binding sites between HNO_3 and iodine oxoacids, we analyzed their molecular electrostatic potential (ESP, Figure S1), which maps the electron-rich (electronegative) and electron-deficient (electropositive) regions on the molecular surface, where noncovalent bonds are prone to form. The ESP analysis indicates that HNO_3 can interact with iodine oxoacids through diverse bonding modes, reflecting its dual role as both a halogen bond acceptor and a hydrogen bond donor. For halogen bonding, the nitro oxygen atoms of

HNO_3 exhibit a localized negative ESP (-18.7 kcal mol^{-1}), providing accessible sites to accept halogen bonds from the electrophilic iodine centers of HIO_3 and HIO_2. More importantly, the hydroxyl hydrogen of HNO_3 displays a highly positive ESP (+67.9 kcal mol^{-1}), which is significantly more electropositive than the hydroxyl hydrogen sites in HIO_3 (+59.1 kcal mol^{-1}) or HIO_2 (+57.3 kcal mol^{-1}). This enhanced electropositivity enables HNO_3 to act as a superior proton donor, favoring proton transfer to the electron-rich site during cluster formation.

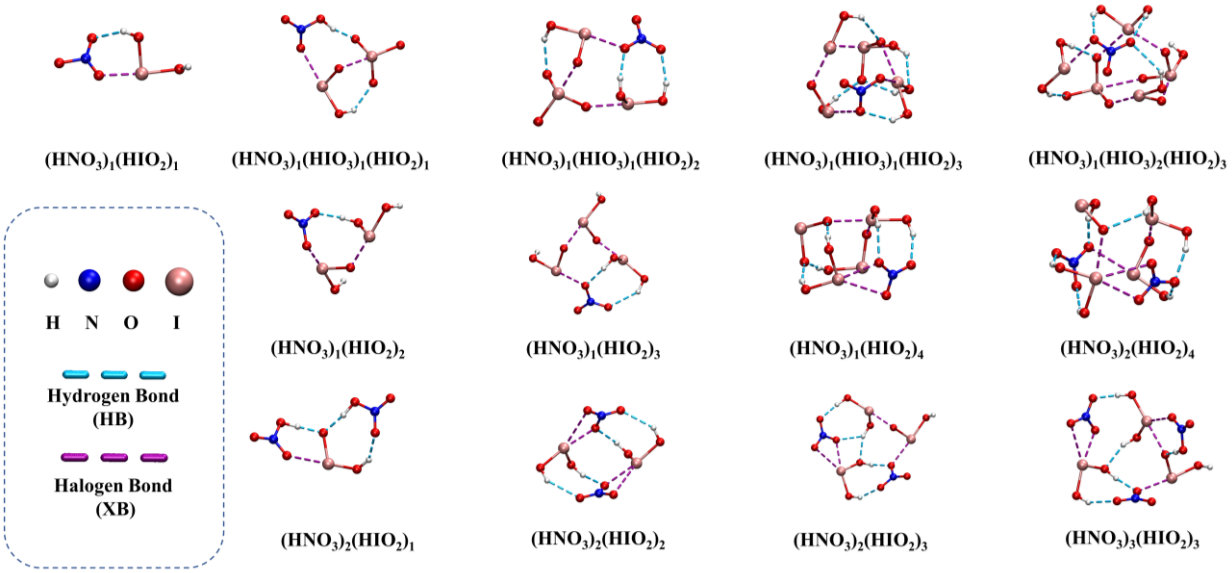

Figure 1. Representative most stable structures of HNO_3–HIO_3–HIO_2 clusters identified at the ωB97X-D/6-311++G (3df, 3pd) (for H, N, and O atoms) and aug-cc-pVTZ-PP with ECP28MDF (for I atom) levels of theory. The complete set of all identified structures is provided in Figure S2. The white, blue, red, and pink balls represent the H, N, O, and I atoms, respectively. The hydrogen bonds and halogen bonds are shown in dashed blue and purple lines, respectively.

To confirm the dominant binding modes, we employed a multi-step conformational search strategy, we identified the most stable configurations of $(HNO_3)_x(HIO_3)_y(HIO_2)_z$ clusters ($2 \le x + y + z \le 6$, $1 \le x \le 3$) as shown in Figure 1. In these optimized clusters, HNO_3 molecules form thermodynamically stable structures with iodine oxoacids (HIO_3/HIO_2) via an interaction network bridged by hydrogen bonds and halogen bonds. Within this ternary system, HNO_3 and HIO_3 act as proton donors (acids), while HIO_2 serves as the proton acceptor (base) due to its stronger basicity relative to the acids. Both HNO_3 and HIO_3 undergo proton transfer to HIO_2, thereby forming ion pairs that substantially enhance cluster stability by strengthening electrostatic interactions.

To quantitatively characterize the strength of these intermolecular interactions, we performed AIM analysis (Table S2). The results confirm that HNO_3 acts primarily as a hydrogen bond donor rather than a halogen bond acceptor. HNO_3 accounts for 80% of all HBs, the majority of which are medium-strength bonds (Emamian et al., 2019) (68.3% exhibit binding energies of 12.0–24.0 kcal mol^{-1}, with $\nabla^2\rho(r) > 0$ and $H(r) < 0$). These HBs are comparable in strength to those formed between iodine

oxoacids themselves, highlighting HNO_3's contribution to the hydrogen bonding network. By comparison, HNO_3 contributes 37% of all XBs in the ternary clusters. The N–O···I XBs formed between HNO_3 and iodine oxoacids are weaker (average $\rho(r)$: 0.036 a.u.; average bond length: 2.7 Å) than the XBs formed between iodine oxoacids (average $\rho(r)$: 0.054 a.u.; average bond length: 2.4 Å).

3.2 Cluster Stability

To elucidate the stability of the HNO_3-HIO_3-HIO_2 clusters, we evaluated their thermodynamic and kinetic properties (Figure 2). Thermodynamic analysis reveals a distinct acid-base stoichiometry dependence of cluster stability (Figure 2(a)). Consistent with established thermodynamic patterns in acid-base clustering (Olenius et al., 2013; Elm, 2017), six-molecule clusters with an acid-to-base ratio of 1:1 (HNO_3 and HIO_3 as acids, HIO_2 as base) exhibit the lowest Gibbs free energies of formation (ΔG). This 1:1 stoichiometry preference is consistent across all cluster sizes (Figure S3). Notably, for clusters with fixed number of molecules and acid-base ratio, increasing the HNO_3 fraction elevates ΔG across all sizes (Figure S3). This trend indicates that HNO_3–HIO_2 clusters and HNO_3–HIO_3–HIO_2 clusters are less thermodynamically stable than HIO_3–HIO_2 clusters, reflecting the combined effects of hydrogen bonding and halogen bonding on overall cluster stability.

While negative ΔG reflects the thermodynamic feasibility of cluster formation, the kinetic competition between collision–driven growth and evaporation–driven dissociation ultimately determines whether clusters can persist and grow into larger clusters. To assess kinetic feasibility, we calculated the minimum HNO_3 concentration required for clusters to achieve kinetic stability ($\beta c_{boundary}/\Sigma\gamma = 1$, where collision rate equals evaporation rate) across tropospheric temperatures (228–288 K, Figure 2(b)) (Dunne et al., 2016; Williamson et al., 2019). Above $c_{boundary}$, cluster growth dominates over dissociation, enabling persistent nucleation.

For HNO_3-containing clusters, ambient HNO_3 concentrations (10^8–10^{11} molecules cm^{-3}), spanning clean polar regions to polluted coastal environments, universally exceed the $c_{boundary}$ across all tropospheric temperatures. This confirms that HNO_3-containing clusters are kinetically viable for growth under real atmospheric conditions. Critical to our altitude-dependent hypothesis, $c_{boundary}$ decreases sharply with declining temperature (Figure 2(b)). For the $(HNO_3)_1(HIO_3)_2(HIO_2)_3$ cluster, $c_{boundary}$ drops from ~10^9 molecules cm^{-3} at 288 K (MBL) to ~10^5 molecules cm^{-3} at 228 K (UT). This four-order-of-magnitude reduction demonstrates that high-altitude low temperatures drastically suppress cluster evaporation, allowing HNO_3 to more effectively stabilize clusters by lowering the concentration threshold for kinetic stability.

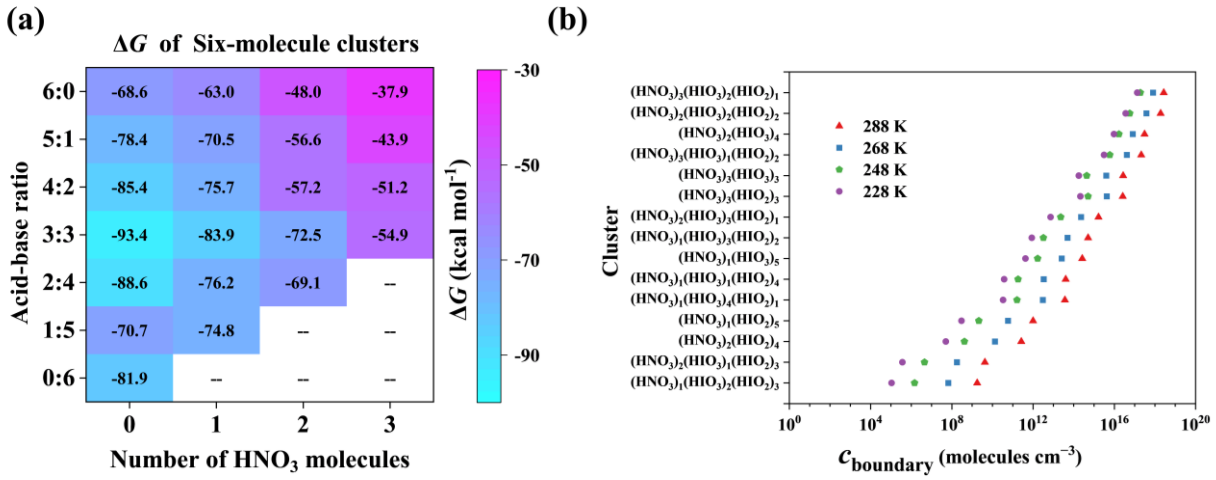

Figure 2. (a) Gibbs free energies of formation (ΔG, kcal mol^{-1}) for the most stable six-molecule HNO_3–HIO_3–HIO_2 clusters at the DLPNO-CCSD(T)/aug-cc-pVTZ(-PP)//ωB97X-D/6-311++G(3df,3pd) + aug-cc-pVTZ-PP level of theory (288 K). (b) Minimum HNO_3 concentrations ($c_{boundary}$) required for six-molecule clusters to reach kinetic stability at various tropospheric temperatures, defined by the condition where the collision frequency equals the total evaporation coefficients ($\beta c_{boundary} = \Sigma\gamma$). Clusters are sorted in ascending order of $c_{boundary}$. Since pure iodine oxoacid clusters, such as $(HIO_3)_3(HIO_2)_3$, do not contain HNO_3, their evaporation rates cannot substitute for those of the clusters formed upon collision with HNO_3. Consequently, the $c_{boundary}$ values for these HNO_3-free clusters are not provided here. Figure S4 presents data for clusters collisions involving other monomers (HIO_3 and HIO_2).

3.3 Cluster Formation Rates under Different Atmospheric conditions

The widespread coexistence of HNO_3 and iodine oxoacids (HIO_3/HIO_2) across diverse atmospheric environments, from polluted coastal MBL to remote UT, motivates a systematic investigation of the cluster formation rate (J) of the HNO_3–HIO_3–HIO_2 ternary system under altitude-resolved tropospheric conditions (Figure 3), focusing on how HIO_3's contribution to J evolves with altitude. We selected four temperatures strictly matching tropospheric vertical gradients: 288 K (MBL), 268 K (polar boundary layer), 248 K (FT), and 228 K (UT) (Dunne et al., 2016). The condensation sink (CS), which quantifies cluster scavenging, was set to 1×10^{-2} s^{-1} (polluted MBL, high background aerosols) and 1×10^{-4} s^{-1} (clean UT, low background aerosols) (Ranjithkumar et al., 2021), directly reflecting observed CS vertical trends. HNO_3 concentrations were set to 10^8–10^{11} molecules cm^{-3} (from remote polar regions (Honrath et al., 2002; Jones et al., 2014) to polluted coastal areas (Xu et al., 2018)), and HIO_3 concentrations ranged between 10^5 and 10^8 molecules cm^{-3} (from inland to coastal environments), mirroring their observed environmental gradients (Sipilä et al., 2016). Given that HIO_2 and HIO_3 are homologous iodine species with co-varying concentrations, [HIO_2] was defined as a fraction of [HIO_3]. Reported [HIO_3]/[HIO_2] ratios range from ~20 to 100 (Sipilä et al., 2016; Baccarini et al., 2020; He et al., 2023), and we adopted a ratio of 50, consistent with field observations at Mace Head (Sipilä et al., 2016) and our previous studies (Li et al., 2024b; Zu et al., 2023, 2024).

High-altitude environments drastically boost the ternary nucleation efficiency via the synergistic decline of temperature and CS with altitude. Thermodynamically, lower temperatures suppress cluster evaporation. At a constant CS ($[HNO_3] = 10^{10}$ molecules cm^{-3}, and $[HIO_3] = 10^7$ molecules cm^{-3}), the temperature decline from MBL (288 K) to UT (228 K) enhances J by more than four orders of magnitude (from ~ 10^1 to ~10^5 cm^{-3} s^{-1}). Kinetically, the CS reduction from 1×10^{-2} s^{-1} (polluted lower atmosphere) to 1×10^{-4} s^{-1} (clean UT) minimizes scavenging of nascent clusters. This enhancement is especially important at low iodine oxoacid and HNO_3 concentrations, where clusters form slowly and are therefore more easily scavenged.

Moreover, J exhibits a strong dependence on the concentrations of HNO_3 and iodine oxoacids. As expected, higher precursor concentrations lead to higher J. Notably, the system's sensitivity to nucleation precursor concentrations is strongly altitude-dependent, as visualized by J contour orientations (Figure 3). In the MBL (e.g., 288 K), contours are nearly vertical, which indicates iodine oxoacids dominate nucleation, and HNO_3 only effectively enhances J at high HNO_3 concentrations (> 10^{10} molecules cm^{-3}). In contrast, as temperature decreases with increasing altitude, the contours gradually pivot towards the $[HNO_3]$ axis. At typical UT temperatures (e.g., 228 K), the contour slope approaches -1 across all simulated CS values, demonstrating that HNO_3 exerts a pronounced influence over a broader concentration range than at lower altitudes. Consistent with this, HNO_3's enhancement factor rises to ~10^2 in the UT (Figure S5), confirming its transition to a critical contributor to nucleation. Given the ppb-level HNO_3 concentrations observed in the UT, this enhanced sensitivity underscores the amplified importance of HNO_3 in iodine oxoacid nucleation at high altitudes.

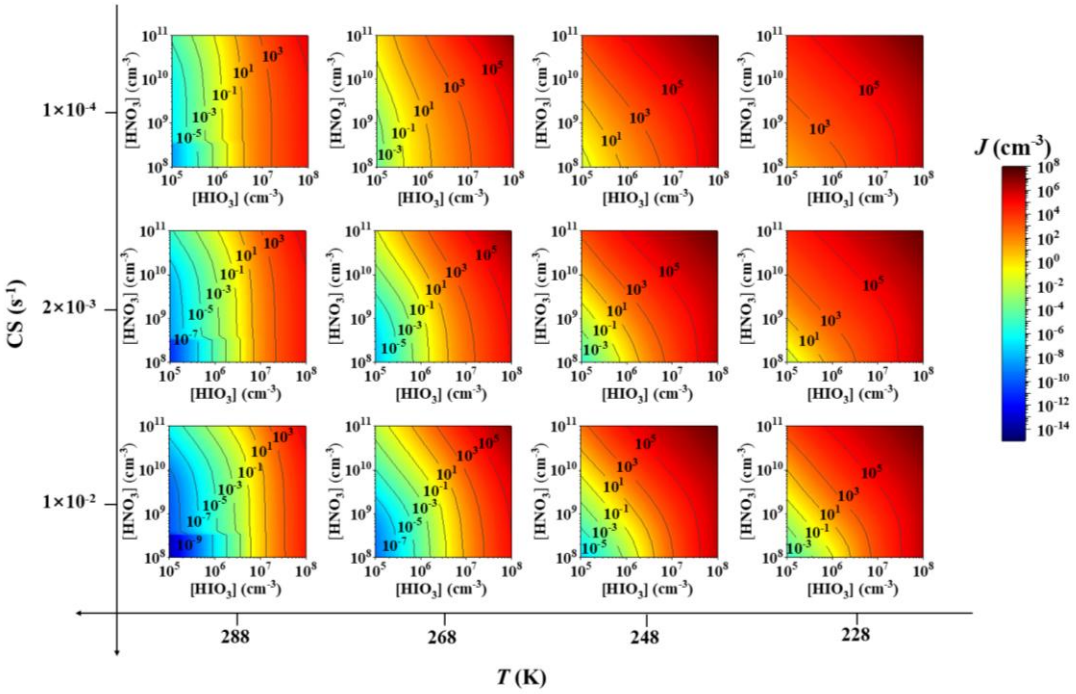

Figure 3. Heatmaps of cluster formation rates (J, in $cm^{-3}\ s^{-1}$) as a function of HNO_3 and HIO_3 concentrations, simulated under various temperature (T) and CS conditions. The HIO_2 concentration was set to [HIO_3]/50. J is represented by a color gradient from blue (10^{-13} cm^{-3} s^{-1}) to red (10^{7} cm^{-3} s^{-1}), with contour lines indicating J values of 10^{-9}, 10^{-7}, 10^{-5}, 10^{-3}, 10^{1}, 10^{3}, and 10^{5} cm^{-3} s^{-1}.

High-altitude regions are critical for nucleation, as they significantly influence global CCN (Gordon et al., 2017). While HNO_3's regulatory role is expected to be altitude-dependent, its quantitative variation across the troposphere remains unclear. To address this gap, we quantified the HNO_3–HIO_3–HIO_2 nucleation mechanism by simulating the evolution of its J along idealized and representative vertical atmospheric profiles. For clarity and ease of discussion, the vertical atmosphere was approximately stratified into the MBL (0–2 km), FT (2–12 km), and UT, (12–14 km), matching the concentration distributions of the nucleation precursors at different altitudes in the atmosphere (Jurkat et al., 2014).

A uniform temperature lapse rate of 6 K km^{-1} (starting from 288 K at the surface) (Catling and Kasting, 2017) and a CS decline from 2×10^{-3} to 1×10^{-4} s^{-1} (Ranjithkumar et al., 2021), were applied to reflect the transition from particle–rich MBL to clean FT. Precursor vertical concentrations were constrained as follows: the HNO_3 concentration was set to 1×10^{10} molecules cm^{-3} in the MBL (anthropogenic coastal conditions), decreasing to 1×10^{9} molecules cm^{-3} in the FT, and increasing to a constant 5×10^{9} molecules cm^{-3} (sub-ppb to ppb level) in the UT (Jurkat et al., 2014). HIO_3 concentration was set to 1×10^{7} molecules cm^{-3} in the MBL (coastal emission hotspot) (Sipilä et al., 2016) and reduced by one order of magnitude in the FT. Due to limited field constraints on HIO_3 at high altitudes, its concentration was held constant above the FT. This assumption is based on the fact that the concentration of iodine monoxide (IO) radical, a key precursor of HIO_3 in the troposphere with relatively stable concentrations across altitudes (Koenig et al., 2020; Finkenzeller et al., 2023), exhibits an observed positive correlation with that of HIO_3 in the troposphere (Koenig et al., 2020; Finkenzeller et al., 2023). HIO_2 concentration was fixed at a ratio of 1/50 relative to HIO_3 across all altitudes, consistent with the conditions in Figure 3.

Based on the above constrained simulation conditions, we partitioned the altitude–dependent evolution of J into four stages (Figure 4(e, f)). In Stage 1 (0–2 km, from the MBL to the lower FT), as altitude increases, the suppressive effects of decreasing HNO_3 and HIO_3 concentrations outweigh the promoting effects of lower temperature and reduced CS, resulting in a J minimum. Near 2 km, J is ~70-fold lower than that in the MBL. At this stage, the enhancement factor of HNO_3 (R, defined as J(HNO_3–HIO_3–HIO_2)/J(HIO_3–HIO_2)) is approximately 1.5–2, which indicates a modest promotional effect of HNO_3. In Stage 2 (2–12 km, FT), with precursor concentrations held constant, the continuous decline in temperature emerges as the dominant driver, boosting J for both the binary (HIO_3–HIO_2) and ternary (HNO_3–HIO_3–HIO_2) mechanisms. Notably, the ternary mechanism shows a steeper altitude-dependent increase in J, reflecting stronger HNO_3 stabilization at low temperatures, with R reaching 10^2 at 8 km. Comparison of altitude–dependent trends reveals distinct "sensitive zones" where J responds most sharply to altitude. For the binary HIO_3–HIO_2 mechanism, this zone is confined to a relatively narrow layer (8–10 km). By comparison, the J of the ternary HNO_3–HIO_3–HIO_2 mechanism not only achieves a higher peak but also sustains rapid growth over a broader vertical range (2–8 km), highlighting its efficacy across a wider altitude span. In Stage 3 (12–13 km, UT), J becomes less sensitive to further temperature decreases (Figure S6). At these ultra-low temperatures,

thermodynamically favorable HNO_3-containing clusters (e.g., HNO_3–HIO_2 clusters) are effectively stabilized against evaporation (Figure 2(b)), while elevated UT HNO_3 becomes the key driver of enhancement. Under these conditions, the elevated HNO_3 concentrations in the UT, sustained by lightning–driven chemical production and long–range transport, become the key driver of *R* for HIO_3–HIO_2 nucleation, further elevating *R*. In Stage 4 (13–14 km, upper UT), *J* approaches a steady state as HNO_3 concentrations stabilize at ppb levels and temperature effects saturate.

Overall, *J* for both HIO_3–HIO_2 and HNO_3–HIO_3–HIO_2 mechanisms exhibit non-monotonic altitude profiles, declining from the MBL to ~2 km then increasing toward the UT. Critically, while HNO_3's enhancement on *J* is modest at lower altitudes, its influence increases significantly with altitude, particularly in the UT where the synergy of elevated HNO_3 concentrations and ultra-low temperatures strongly accelerates *J*. Deep convective systems can actively transport iodine oxoacids upward into the UT (Twohy et al., 2002; Randel et al., 2010; Williamson et al., 2019), while lightning-driven oxidation sustains ppb-level HNO_3; conversely, UT-nucleated particles may descend via large-scale subsidence to replenish lower-tropospheric CCN (Wang et al., 2016; Xiao et al., 2023; Mehra et al., 2026). Through this bidirectional vertical coupling, HNO_3 acts as a bridge between marine iodine emissions at the surface and particle formation across the full tropospheric column.

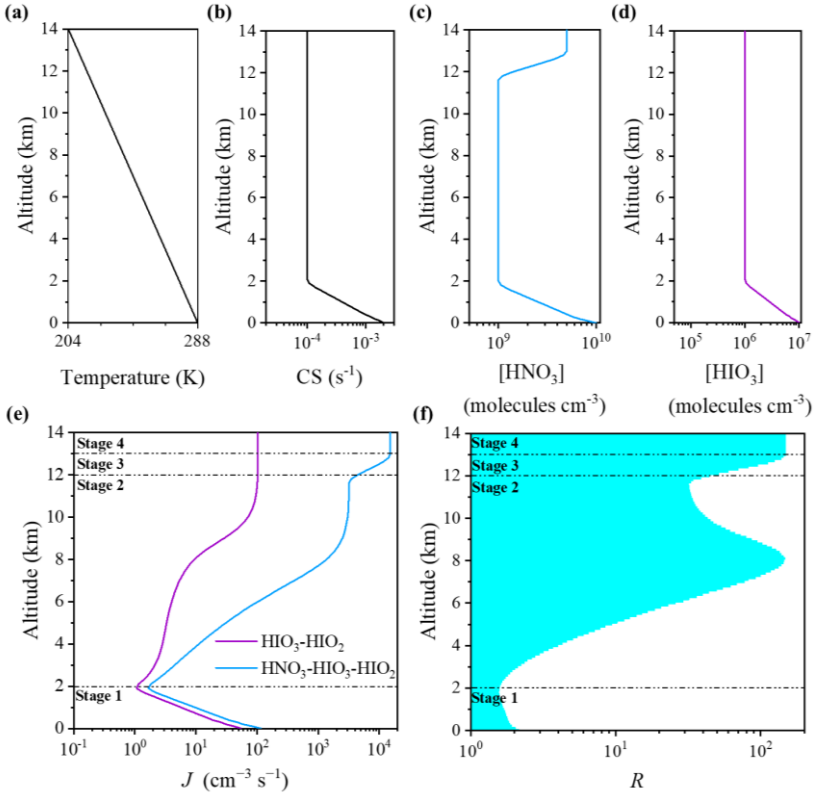

Figure 4. Altitude-dependent simulation inputs and the corresponding cluster formation rates (*J*, cm^{-3} s^{-1}). (a) Temperature; (b) CS; (c) HNO_3 concentration; and (d) HIO_3 concentration as functions of altitude. (e) *J* versus altitude for the HIO_3–HIO_2 (purple) and HNO_3–HIO_3–

HIO_2 (blue) mechanisms, simulated under the vertical profiles in (a–d); dashed lines denote boundaries of the four altitude stages. (f) Altitude-dependent enhancement factor of HNO_3 (R, $J(HNO_3–HIO_3–HIO_2)/J(HIO_3–HIO_2)$) of $HIO_3–HIO_2$ nucleation by HNO_3.

3.4 Altitude-Dependent Nucleation Mechanisms

To uncover the molecular origin of HNO_3's altitude-dependent enhancement, we analyzed the nucleation pathways of the $HNO_3–HIO_3–HIO_2$ system (Figure 5). As illustrated in Figure 5(a), ACDC simulations identify three primary nucleation routes: the binary $HIO_3–HIO_2$ pathway, the ternary $HNO_3–HIO_3–HIO_2$ pathway, and the binary $HNO_3–HIO_2$ pathway. Their branching ratios evolve systematically with altitude, with HNO_3-involved pathways gaining dominance at higher altitude, directly reflecting HNO_3's role transition (Figure 5(b)). Specifically, the binary $HIO_3–HIO_2$ pathway dominates at 0–6 km; above 6 km, the ternary $HNO_3–HIO_3–HIO_2$ pathway takes the lead, while the binary $HNO_3–HIO_2$ pathway also begins to contribute. In the UT, the high concentration of HNO_3 drives the binary $HNO_3–HIO_2$ pathway to become predominant.

HNO_3 promotes nucleation via both direct and indirect pathways. Directly, as a core component, HNO_3 is stably incorporated into growing clusters. For instance, in the binary $HNO_3–HIO_2$ pathway, nucleation proceeds via the stepwise addition of $(HNO_3)_1(HIO_2)_1$ dimers to form $(HNO_3)_2(HIO_2)_2$ tetramers, which subsequently collide to exceed cluster size. Additionally, HNO_3 participates in forming kinetically stable clusters (e.g., $(HNO_3)_1(HIO_3)_2(HIO_2)_3$, $(HNO_3)_2(HIO_3)_1(HIO_2)_3$, and $(HNO_3)_2(HIO_2)_4$). Indirectly, as a catalyst, HNO_3 promotes nucleation via a collision–re-evaporation cycle. Specifically, HNO_3 forms intermediates with HIO_2 (e.g., $(HNO_3)_1(HIO_2)_1$). When these intermediates collide with iodine-containing clusters, HNO_3 molecule re-evaporates into the gas phase while HIO_2 is retained, efficiently transferring HIO_2 to particles and accelerating nucleation.

To further elucidate HNO_3's role across altitudes, Figure 5(c) presents the weighted average molecular composition of outflux clusters (weighted by pathway branching ratios), capturing its altitude-driven functional shift. In the low-to-mid troposphere (0–6 km), HNO_3 constitutes <10% of outflux clusters (dominated by HIO_3/HIO_2), confirming its catalytic role (collision-re-evaporation cycle), resulting in modest enhancement (< 10-fold). Above 6 km, the proportion of HNO_3 in outflux clusters rises steadily, exceeding 40% in the UT, signaling its transition to a core component. This shift is accompanied by a much more significant promotional effect, with R reaching up to 200-fold (Figure 4(f)).

The altitude-dependent role transition of HNO_3 is driven by the different temperature sensitivities of evaporation (far more sensitive) versus collision coefficients (Supplementary Methods). This temperature sensitivity leads to fundamentally different nucleation behaviors: at low altitudes, rapid evaporation ensures that only the most thermodynamically stable clusters survive; at high altitudes, suppressed evaporation shifts the controlling factor to precursor availability.

At low altitudes (MBL), evaporation-limited conditions favor 1:1 acid-base stoichiometry (minimal evaporation rates, Figure 5(c)) in both binary $HIO_3–HIO_2$ and ternary $HNO_3–HIO_3–HIO_2$ pathways. With increasing altitude and decreasing temperature, evaporation is suppressed and nucleation becomes collision-limited, favouring the most abundant species. For ternary nucleation mechanism, high HNO_3 concentrations (exceeding iodine oxoacids) drive more frequent $HNO_3–HIO_2$ collisions, making HNO_3–involved pathways dominant in the UT (Figure 5(b)).

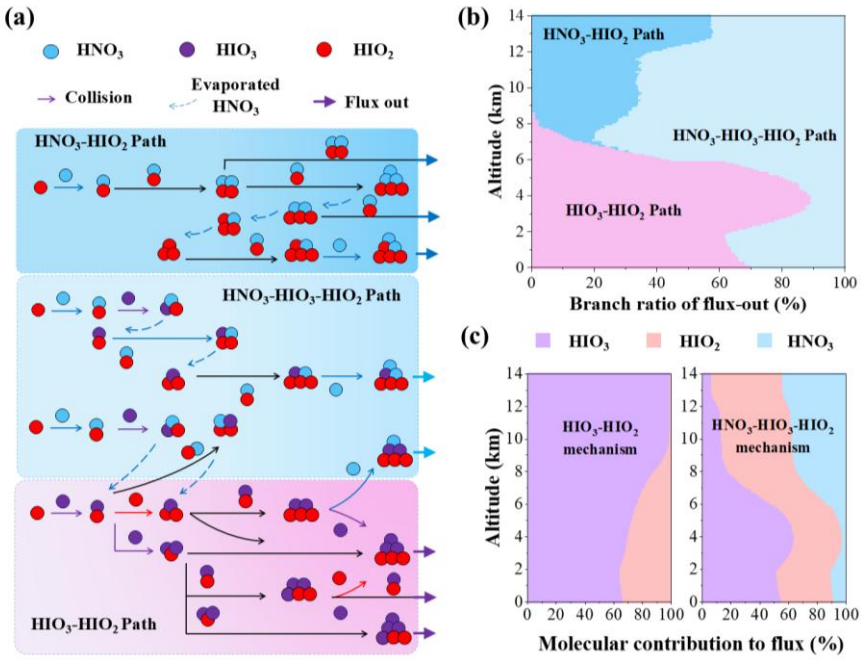

Figure 5. Altitude-dependent nucleation pathways and cluster composition under atmospheric conditions in Figure 4. (a) Three primary nucleation pathways identified by ACDC simulations: binary HIO_3–HIO_2, ternary HNO_3–HIO_3–HIO_2, and binary HNO_3–HIO_2 pathway. (b) Branching ratios of the flux out for three nucleation pathways at different altitudes. (c) Number contributions of HNO_3, HIO_3, and HIO_2 molecules to the total outflux clusters at different altitudes. Left: HIO_3–HIO_2 mechanism; Right: HNO_3–HIO_3–HIO_2 mechanism.

3.5 Comparison with Typical Nucleation Systems

To assess the atmospheric significance of the proposed HNO_3–HIO_3–HIO_2 mechanism and identify the specific environments where it plays a role, we compared it against well-established nucleation mechanisms. We selected four representative environments: a polluted coastal area (Zhejiang, China), a clean marine site (Mace Head, Ireland), a polar region (Greenland), and UT, encompassing pollution gradients (polluted-to-clean) and temperature ranges (high-to-low) to cover the core application scenarios of the nucleation mechanism. The comparison analysis included three key mechanisms: (1) the binary HIO_3–HIO_2 nucleation (purple dashed line, as a baseline), (2) the ternary HNO_3–HIO_3–HIO_2 nucleation proposed in this study (blue solid and dashed lines), and (3) the competing H_2SO_4-driven mechanism (i.e., H_2SO_4–DMA (Kürten et al., 2013) for polluted coastal regions or H_2SO_4–NH_3–HNO_3 for the UT (Wang et al., 2022)) (red solid line). All data (Liu et al., 2018, 2021, 2023) related to quantum chemical calculations of the mechanisms were re-calculated at the same level of theory to ensure the result comparability.

For the polluted coastal environment of Zhejiang (Figure 6(a), 288 K, CS = 1.0×10^{-2} s^{-1} (Ning et al., 2022), [HIO_3] = 5×10^6 molecules cm^{-3} (He et al., 2021),) HNO_3 at the typical concentration (Xu et al., 2018) of 1×10^{10} molecules cm^{-3} can

enhance HIO_3–HIO_2 nucleation by 10-fold, consistent with its catalytic role in the MBL. Under extremely polluted conditions ([HNO_3] = 1×10^{11} molecules cm^{-3}), this enhancement reaches 10^2-fold, enabling the HNO_3–HIO_3–HIO_2 mechanism to achieve better agreement with field observations (Yu et al., 2019) (gray shaded area in Figure 6(a)). With ongoing global sulfur emission reductions, the HNO_3–HIO_3–HIO_2 mechanism emerges as an increasingly significant, and potentially dominant, pathway for NPF in polluted coastal regions. At the clean coastal site of Mace Head (Figure 6(b), 288 K, CS = 2.0×10^{-3} s^{-1}) (Sipilä et al., 2016), elevated ambient [HIO_3] (Heard et al., 2006) limits HNO_3's contribution, leading to modest enhancement (<1.5-fold). Both the HNO_3–HIO_3–HIO_2 and HIO_3–HIO_2 mechanisms generally reach, and at higher concentrations modestly exceed, the upper limit of field-observed cluster formation rates. This potential overestimation of J likely originates from methodological limitations: specifically, the finite seven-molecule boundary may not encompass the critical cluster size (Besel et al., 2020), and the applied quantum chemical level of theory might inherently produce slightly overbound clusters (Engsvang et al., 2024).

With decreasing temperature or increasing altitude, the enhancement effect of HNO_3 on HIO_3–HIO_2 nucleation becomes progressively pronounced. In the cold polar environment of Greenland (Figure 6(c), 268K, CS = 1.0×10^{-4} s^{-1}), an [HIO_3] of 10^6–10^7 (Baccarini et al., 2020), HNO_3 can provide an enhancement of ~2–3 times at typical ambient HNO_3 concentrations (e.g., 10^9 molecules cm^{-3}) (Honrath et al., 2002). However, with increasing anthropogenic NO_x emissions from shipping activities due to Arctic warming (Dalsøren et al., 2013; Gong et al., 2018; Qi et al., 2024), local HNO_3 concentrations may rise significantly. Our simulations show that if local [HNO_3] reaches 10^{10} molecules cm^{-3}, the cluster formation rate of the HNO_3-HIO_3-HIO_2 mechanism can reach up to 10^2–10^4 cm^{-3} s^{-1}, an enhancement of 20-fold compared to the binary HIO_3-HIO_2 mechanism. Under cold Arctic conditions with a low condensation sink, cluster evaporation and scavenging losses are strongly suppressed, allowing HNO_3 to participate more effectively in cluster stabilization. Consequently, modest increases in HNO_3 concentrations from rising shipping NO_x emissions translate directly into substantial enhancements in the cluster formation rate. This significant enhancement highlights the potential importance of this mechanism for local NPF under the influence of high concentrations of anthropogenic NO_x.

In the UT (Figure 6(d), 228 K, CS = 1.0×10^{-4} s^{-1}) (Williamson et al., 2019), conventional pathways (e.g., pure HIO_3–HIO_2 nucleation) are inefficient (10^{-3} cm^{-3} s^{-1} < J < 10^2 cm^{-3} s^{-1}). However, at the observed HNO_3 concentrations in the UT (~ppb levels, i.e., [HNO_3] = 5×10^9 molecules cm^{-3}) (Jurkat et al., 2014), J increases to 10^3–10^4 cm^{-3} s^{-1}, an enhancement of 10^2 to 10^6 times over the pure HIO_3–HIO_2 mechanism, establishing HNO_3 as a core component of UT nucleation clusters. This rate far exceeds that of the reported H_2SO_4–NH_3–HNO_3 mechanism in this region (1–100 cm^{-3} s^{-1}), establishing HNO_3–HIO_3–HIO_2 nucleation as the potentially critical nucleation pathway in the UT, supported by the enhanced stability of HNO_3–HIO_2 clusters at low temperatures (Tables S4 and S5).

In summary, the enhancement of HIO_3–HIO_2 nucleation by HNO_3 is widespread across diverse atmospheric environments, and it emerges as a potentially dominant mechanism under high–altitude or low–temperature conditions, consistent with its altitude-dependent functional transition from MBL catalyst to UT core component. In the context of SO_2 emission reductions,

the high atmospheric abundance and broad spatial distribution of HNO_3 are anticipated to exert a profound and far-reaching impact on global NPF, highlighting the need to incorporate its altitude-dependent role into atmospheric models.

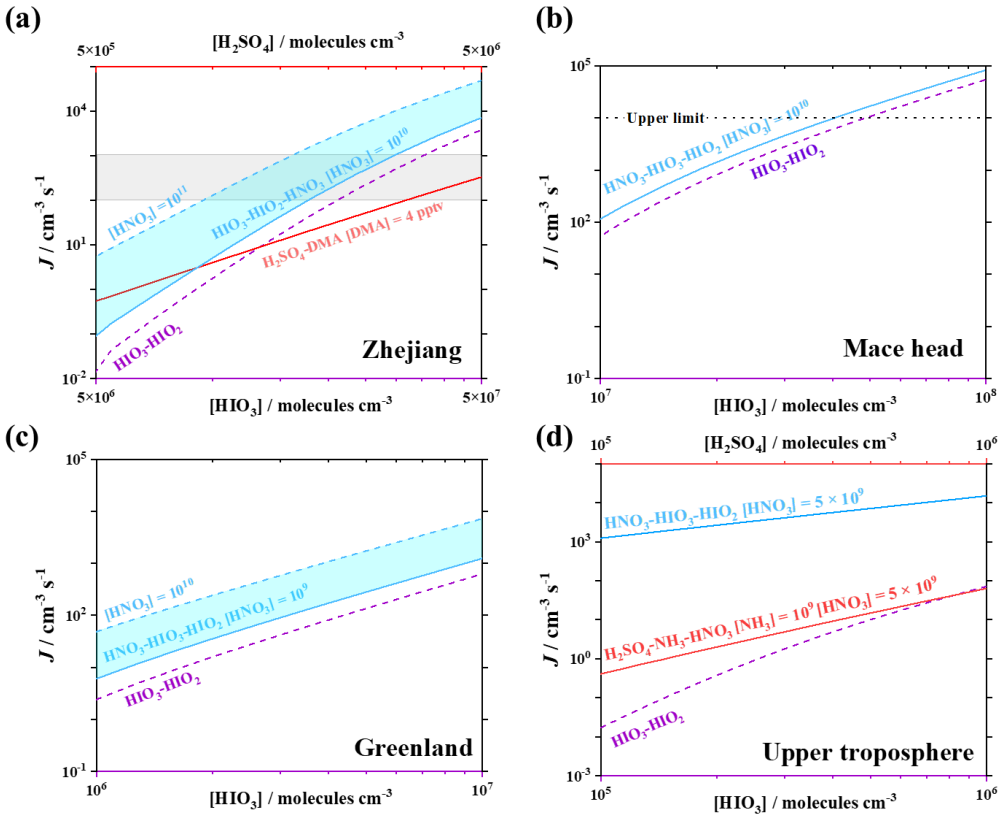

Figure 6. Cluster formation rates (J, cm^{-3} s^{-1}) for HIO_3–HIO_2 (purple dashed line), HNO_3–HIO_3–HIO_2 (blue) and H_2SO_4–DMA or H_2SO_4–NH_3–HNO_3 (red) systems under the corresponding atmospheric conditions in (a) Zhejiang, where gray shaded areas represent locally observed cluster formation rates (Yu et al., 2019); (b) Mace Head, where the dashed line marks the upper limit of cluster formation rates reported in field observations (Sipilä et al., 2016); (c) Greenland; and (d) the UT.

3.6 Uncertainty Analysis

To evaluate the robustness of our results, specifically HNO_3's altitude-dependent transition from MBL catalyst to UT core component, we systematically analyzed uncertainties arising from two primary sources: quantum chemical calculations of Gibbs free energies of cluster formation (ΔG) and the atmospheric constraints on precursor concentrations (HIO_3 and HIO_2).

Regarding quantum chemical calculations, we examined the sensitivity of J to calculated ΔG variations by applying ±1 kcal mol^{-1} perturbations to all clusters (Figure S8), a magnitude consistent with prior benchmarks showing that DLPNO-CCSD(T) typically exhibits a potential ΔE error of < 1 kcal mol^{-1} relative to CCSD(F12*)/CBS results (Schmitz and Elm, 2020). These perturbations directly affect cluster stability: a +1 kcal mol^{-1} shift destabilizes clusters and increases evaporation rates into monomers, while a -1 kcal mol^{-1} shift enhances stabilization against evaporation (evaporation rate coefficient γ in eq

S2). Under MBL conditions, where HNO_3 acts primarily as a catalyst and cluster evaporation is inherently rapid, these perturbations significantly affect the enhancement factor (R) of HNO_3: +1 kcal mol^{-1} shift reduces R to < 2, while -1 kcal mol^{-1} shift increases it to > 10 (baseline R = 2–3). As indicated by prior benchmarks (Schmitz and Elm, 2020; Engsvang et al., 2024), the DLPNO-CCSD(T) method may slightly underestimate ΔG (i.e., over-bind the clusters). Therefore, the +1 kcal mol^{-1} perturbation is likely the most realistic scenario. Notably, this sensitivity diminishes rapidly with the increasing altitude. In the UT, where HNO_3 serves as a core component and its evaporation is effectively suppressed, the impact of ΔG perturbations on J becomes negligible. This altitude-dependent sensitivity not only validates HNO_3's functional transition (from MBL catalyst to UT core component), but also confirms its robust enhancement at high altitudes.

We further conducted sensitivity tests for the concentrations of HIO_2 and HIO_3 (Figures S9 and S10) to assess the mechanism's applicability across varying atmospheric conditions. Consistent with the flux composition (Figure 5(c)), the HNO_3–HIO_3–HIO_2 mechanism shows strong sensitivity to HIO_2 concentrations: HNO_3 enhances nucleation even at low [HIO_2], both J and R increase substantially with HIO_2 abundance. Although atmospheric HIO_2 concentrations remain poorly constrained, our simulated concentration ranges are consistent with CLOUD chamber observations under UT conditions (Shen et al., 2024). Furthermore, theoretical studies have confirmed HIO_2's stability against tropospheric photolysis (De Souza and Brown, 2014) and oxidation (Khanniche et al., 2017), supporting the mechanism's robustness under realistic conditions.

It is also worth noting the potential uncertainties related to the relativistic effects. A recent benchmark (Engsvang et al., 2024) has demonstrated that the ZORA-DLPNO-CCSD(T) approach, which incorporates the zeroth-order regular approximation (ZORA) (Lenthe et al., 1993) provides thermodynamic estimates that are highly consistent with reference ZORA-CCSD(T) calculations. To address this, we performed single-point energy calculations at the ZORA-DLPNO-CCSD(T)/ma-ZORA-def2-TZVPP (for H, N, and O) (Neese, 2012) + SARC-ZORA-TZVPP (for I) (Rolfes et al., 2020) level of theory using the ORCA program. To provide more precise thermodynamic energies, the ZORA-corrected results are listed in Table S6, and the subsequently simulated J are presented in Figure S11. Although it includes more comprehensive physical corrections, the ZORA-corrected energies tend to yield lower J values than the CLOUD measurements. Given that DLPNO-CCSD(T) method demonstrates closer agreement, we have retained it for single-point correction.

4 Conclusion

This study combines quantum chemical calculations and ACDC simulations, to elucidate the role of HNO_3 in iodine oxoacid nucleation, establishing an altitude-dependent HNO_3–HIO_3–HIO_2 nucleation mechanism. Specifically, at the molecular level, HNO_3 can stabilize HIO_3–HIO_2 clusters through a network of hydrogen bonding, halogen bonding, and proton transfer-driven electrostatic interactions. Thermodynamically, the stability of HNO_3-containing clusters exhibits a strong temperature dependence and increases significantly with decreasing temperature, which directly drives the altitude-dependent functional transition of HNO_3. Kinetically, the J shows a non-monotonic vertical profile governed by temperature, CS, and precursor concentrations.

In the low-altitude MBL, high temperatures drive rapid cluster evaporation, thus restricting HNO_3 to a catalytic role via a collision-re-evaporation cycle that confers modest *J* enhancement (~1.5–2-fold). In the UT, low temperatures strongly suppress evaporation, allowing HNO_3 to serve as a core cluster component. This shift leads to the dominance of HNO_3-involved pathways and boosts the nucleation rate by up to 200-fold relative to the binary HIO_3–HIO_2 mechanism. Consequently, the simulated *J* reaches reaching 10^3–10^4 cm^{-3} s^{-1} in the UT, exceeding the classic H_2SO_4–NH_3–HNO_3 nucleation pathway.

The proposed HNO_3–HIO_3–HIO_2 nucleation mechanism provides a new theoretical perspective for interpreting the intense NPF events in both polluted coastal regions and the upper troposphere. It grows in importance as global sulfur emissions decline, while also becoming relevant to rapid NPF in the Arctic under increasing anthropogenic nitrogen emissions. By mediating iodine nucleation across the troposphere, HNO_3 effectively links marine iodine emissions to troposphere-wide CCN production, with implications for cloud formation and Earth's radiative balance.

These findings highlight the critical need to incorporate altitude-dependent HNO_3-iodine nucleation into global climate and aerosol models. Future work should explore interactions with other atmospheric bases (e.g., ammonia, amines) and acids (e.g., organic acids, methanesulfonic acid), as well as joint laboratory, field, and modeling studies, to further constrain the role of HNO_3 in complex atmospheric environments.

Data availability

The data in this article are available from the corresponding author upon reasonable request (lingliu@bit.edu.cn and zhangxiuhui@bit.edu.cn).

Supplement link

The supplement related to this article is available online at:

Author contributions

XZ designed and supervised the research. JZ, LL and HZ performed the quantum chemical calculations and the ACDC simulations. LL, AN and XZ analyzed data. JZ, LL and XZ wrote the manuscript. HZ, JL, FB, JY and XC, reviewed and edited the manuscript. All authors commented on the paper.

Competing interests

The contact author has declared that neither they nor their co-authors have any competing interests.

Disclaimer

Publisher's note: Copernicus Publications remains neutral with regard to jurisdictional claims in published maps and institutional affiliations.

Acknowledgements

This work was supported by the National Science Fund for Distinguished Young Scholars [grant number 22225607] and the National Natural Science Foundation of China [grant numbers 22376013 and 22306011]. L. Liu thanks the Beijing Institute of Technology Research Fund Program for Young Scholars. We thank for the technical support of the National Large Scientific and Technological Infrastructure "Earth System Numerical Simulation Facility" (https://cstr.cn/31134.02.EL).

Financial support

This work was supported by the National Science Fund for Distinguished Young Scholars [grant number 22225607] and the National Natural Science Foundation of China [grant numbers 22376013 and 22306011]. L. Liu thanks the Beijing Institute of Technology Research Fund Program for Young Scholars.

References

Aas, W., Mortier, A., Bowersox, V., Cherian, R., Faluvegi, G., Fagerli, H., Hand, J., Klimont, Z., Galy-Lacaux, C., Lehmann, C. M. B., Myhre, C. L., Myhre, G., Olivié, D., Sato, K., Quaas, J., Rao, P. S. P., Schulz, M., Shindell, D., Skeie, R. B., Stein, A., Takemura, T., Tsyro, S., Vet, R., and Xu, X.: Global and regional trends of atmospheric sulfur, Sci. Rep., 9, 953, https://doi.org/10.1038/s41598-018-37304-0, 2019.

Baccarini, A., Karlsson, L., Dommen, J., Duplessis, P., Vüllers, J., Brooks, I. M., Saiz-Lopez, A., Salter, M., Tjernström, M., Baltensperger, U., Zieger, P., and Schmale, J.: Frequent new particle formation over the high Arctic pack ice by enhanced iodine emissions, Nat. Commun., 11, 4924, https://doi.org/10.1038/s41467-020-18551-0, 2020.

Bai, X., Lian, Y., Peng, J., Mao, H., and Jiang, S.: Ethylenediamine-Enhanced Iodic Acid Nucleation: Mechanistic Insights into Marine New Particle Formation, Environ. Sci. Technol., 59, 22772–22783, https://doi.org/10.1021/acs.est.5c08562, 2025.

Besel, V., Kubečka, J., Kurtén, T., and Vehkamäki, H.: Impact of Quantum Chemistry Parameter Choices and Cluster Distribution Model Settings on Modeled Atmospheric Particle Formation Rates, J. Phys. Chem. A, 124, 5931–5943, https://doi.org/10.1021/acs.jpca.0c03984, 2020.

Catling, D. C. and Kasting, J. F.: Atmospheric Evolution on Inhabited and Lifeless Worlds, Cambridge University Press, 2017.

Chan, B. and Yim, W.-L.: Accurate Computation of Cohesive Energies for Small to Medium-Sized Gold Clusters, J. Chem. Theory Comput., 9, 1964–1970, https://doi.org/10.1021/ct400047y, 2013.

Cuevas, C. A., Maffezzoli, N., Corella, J. P., Spolaor, A., Vallelonga, P., Kjær, H. A., Simonsen, M., Winstrup, M., Vinther, B., Horvat, C., Fernandez, R. P., Kinnison, D., Lamarque, J.-F., Barbante, C., and Saiz-Lopez, A.: Rapid increase in atmospheric iodine levels in the North Atlantic since the mid-20th century, Nat. Commun., 9, 1452, https://doi.org/10.1038/s41467-018-03756-1, 2018.

Dalsøren, S. B., Samset, B. H., Myhre, G., Corbett, J. J., Minjares, R., Lack, D., and Fuglestvedt, J. S.: Environmental impacts of shipping in 2030 with a particular focus on the Arctic region, Atmos. Chem. Phys., 13, 1941–1955, https://doi.org/10.5194/acp-13-1941-2013, 2013.

De Souza, G. L. C. and Brown, A.: Probing ground and low-lying excited states for HIO_2 isomers, J. Chem. Phys., 141, 234303, https://doi.org/10.1063/1.4903789, 2014.

Dunne, E. M., Gordon, H., Kürten, A., Almeida, J., Duplissy, J., Williamson, C., Ortega, I. K., Pringle, K. J., Adamov, A., Baltensperger, U., Barmet, P., Benduhn, F., Bianchi, F., Breitenlechner, M., Clarke, A., Curtius, J., Dommen, J., Donahue, N. M., Ehrhart, S., Flagan, R. C., Franchin, A., Guida, R., Hakala, J., Hansel, A., Heinritzi, M., Jokinen, T., Kangasluoma, J., Kirkby, J., Kulmala, M., Kupc, A., Lawler, M. J., Lehtipalo, K., Makhmutov, V., Mann, G., Mathot, S., Merikanto, J., Miettinen, P., Nenes, A., Onnela, A., Rap, A., Reddington, C. L. S., Riccobono, F., Richards, N. A. D., Rissanen, M. P., Rondo, L., Sarnela, N., Schobesberger, S., Sengupta, K., Simon, M., Sipilä, M., Smith, J. N., Stozkhov, Y., Tomé, A., Tröstl, J., Wagner, P. E., Wimmer, D., Winkler, P. M., Worsnop, D. R., and Carslaw, K. S.: Global atmospheric particle formation from CERN CLOUD measurements, Science, 354, 1119–1124, https://doi.org/10.1126/science.aaf2649, 2016.

Elm, J.: Elucidating the Limiting Steps in Sulfuric Acid–Base New Particle Formation, J. Phys. Chem. A, 121, 8288–8295, https://doi.org/10.1021/acs.jpca.7b08962, 2017.

Elm, J. and Kristensen, K.: Basis set convergence of the binding energies of strongly hydrogen-bonded atmospheric clusters, Phys. Chem. Chem. Phys., 19, 1122–1133, https://doi.org/10.1039/C6CP06851K, 2017.

Elm, J., Bilde, M., and Mikkelsen, K. V.: Assessment of Density Functional Theory in Predicting Structures and Free Energies of Reaction of Atmospheric Prenucleation Clusters, J. Chem. Theory Comput., 8, 2071–2077, https://doi.org/10.1021/ct300192p, 2012.

Elm, J., Bilde, M., and Mikkelsen, K. V.: Assessment of binding energies of atmospherically relevant clusters, Phys. Chem. Chem. Phys., 15, 16442, https://doi.org/10.1039/c3cp52616j, 2013.

Emamian, S., Lu, T., Kruse, H., and Emamian, H.: Exploring Nature and Predicting Strength of Hydrogen Bonds: A Correlation Analysis Between Atoms-in-Molecules Descriptors, Binding Energies, and Energy Components of Symmetry-Adapted Perturbation Theory, J. Comput. Chem., 40, 2868–2881, https://doi.org/10.1002/jcc.26068, 2019.

Engsvang, M., Wu, H., and Elm, J.: Iodine Clusters in the Atmosphere I: Computational Benchmark and Dimer Formation of Oxyacids and Oxides, ACS Omega, 9, 31521–31532, https://doi.org/10.1021/acsomega.4c01235, 2024.

Fan, J., Wang, Y., Rosenfeld, D., and Liu, X.: Review of Aerosol–Cloud Interactions: Mechanisms, Significance, and Challenges, J. Atmos. Sci., 73, 4221–4252, https://doi.org/10.1175/JAS-D-16-0037.1, 2016.

Finkenzeller, H., Iyer, S., He, X.-C., Simon, M., Koenig, T. K., Lee, C. F., Valiev, R., Hofbauer, V., Amorim, A., Baalbaki, R., Baccarini, A., Beck, L., Bell, D. M., Caudillo, L., Chen, D., Chiu, R., Chu, B., Dada, L., Duplissy, J., Heinritzi, M., Kemppainen, D., Kim, C., Krechmer, J., Kürten, A., Kvashnin, A., Lamkaddam, H., Lee, C. P., Lehtipalo, K., Li, Z., Makhmutov, V., Manninen, H. E., Marie, G., Marten, R., Mauldin, R. L., Mentler, B., Müller, T., Petäjä, T., Philippov, M., Ranjithkumar, A., Rörup, B., Shen, J., Stolzenburg, D., Tauber, C., Tham, Y. J., Tomé, A., Vazquez-Pufleau, M., Wagner, A. C., Wang, D. S., Wang, M., Wang, Y., Weber, S. K., Nie, W., Wu, Y., Xiao, M., Ye, Q., Zauner-Wieczorek, M., Hansel, A., Baltensperger, U., Brioude, J., Curtius, J., Donahue, N. M., Haddad, I. E., Flagan, R. C., Kulmala, M., Kirkby, J., Sipilä, M., Worsnop, D. R., Kurten, T., Rissanen, M., and Volkamer, R.: The gas-phase formation mechanism of iodic acid as an atmospheric aerosol source, Nat. Chem., 15, 129–135, https://doi.org/10.1038/s41557-022-01067-z, 2023.

Francl, M. M., Pietro, W. J., Hehre, W. J., Binkley, J. S., Gordon, M. S., DeFrees, D. J., and Pople, J. A.: Self-consistent molecular orbital methods. XXIII. A polarization-type basis set for second-row elements, J. Chem. Phys., 77, 3654–3665, https://doi.org/10.1063/1.444267, 1982.

Frege, C., Bianchi, F., Molteni, U., Tröstl, J., Junninen, H., Henne, S., Sipilä, M., Herrmann, E., Rossi, M. J., Kulmala, M., Hoyle, C. R., Baltensperger, U., and Dommen, J.: Chemical characterization of atmospheric ions at the high altitude research station Jungfraujoch (Switzerland), Atmos. Chem. Phys., 17, 2613–2629, https://doi.org/10.5194/acp-17-2613-2017, 2017.

Frisch, M. J., Trucks, G. W., Schlegel, H. B., Scuseria, G. E., Robb, M. A., Cheeseman, J. R., Scalmani, G., Barone, V., Mennucci, B., Petersson, G. A., Nakatsuji, H., Caricato, M., Li, X., Hratchian, H. P., Izmaylov, A. F., Bloino, J., Zheng, G., Sonnenberg, J. L., Hada, M., Ehara, M., Toyota, K., Fukuda, R., Hasegawa, J., Ishida, M., Nakajima, T., Honda, Y., Kitao, O., Nakai, H., Vreven, T., Montgomery, J. A., Peralta, J. E., Ogliaro, F., Bearpark, M., Heyd, J. J., Brothers, E., Kudin, K. N., Staroverov, V. N., Kobayashi, R., Normand, J., Raghavachari, K., Rendell, A., Burant, J. C., Iyengar, S. S., Tomasi, J., Cossi, M., Rega, N., Millam, J. M., Klene, M., Knox, J. E., Cross, J. B., Bakken, V., Adamo, C., Jaramillo, J., Gomperts, R., Stratmann, R. E., Yazyev, O., Austin, A. J., Cammi, R., Pomelli, C., Ochterski, J. W., Martin, R. L., Morokuma, K., Zakrzewski, V. G., Voth, G. A., Salvador, P., Dannenberg, J. J., Dapprich, S., Daniels, A. D., Farkas, O., Foresman, J. B., Ortiz, J. V., Cioslowski, J., and Fox, D. J.: Gaussian 16, Revision A.03; Gaussian, Inc.: Wallingford CT, https://gaussian.com/citation_a03/ (last access:19 March 2026), 2016.

Gong, W., Beagley, S. R., Cousineau, S., Sassi, M., Munoz-Alpizar, R., Ménard, S., Racine, J., Zhang, J., Chen, J., Morrison, H., Sharma, S., Huang, L., Bellavance, P., Ly, J., Izdebski, P., Lyons, L., and Holt, R.: Assessing the impact of shipping emissions on air pollution in the Canadian Arctic and northern regions: current and future modelled scenarios, Atmos. Chem. Phys., 18, 16653–16687, https://doi.org/10.5194/acp-18-16653-2018, 2018.

Gordon, H., Kirkby, J., Baltensperger, U., Bianchi, F., Breitenlechner, M., Curtius, J., Dias, A., Dommen, J., Donahue, N. M., Dunne, E. M., Duplissy, J., Ehrhart, S., Flagan, R. C., Frege, C., Fuchs, C., Hansel, A., Hoyle, C. R., Kulmala, M., Kürten, A., Lehtipalo, K., Makhmutov, V., Molteni, U., Rissanen, M. P., Stozkhov, Y., Tröstl, J., Tsagkogeorgas, G., Wagner, R., Williamson, C., Wimmer, D., Winkler, P. M., Yan, C., and Carslaw, K. S.: Causes and importance of new particle formation

in the present-day and preindustrial atmospheres, J. Geophys. Res. Atmos., 122, 8739–8760, https://doi.org/10.1002/2017JD026844, 2017.

Halonen, R., Zapadinsky, E., Kurtén, T., Vehkamäki, H., and Reischl, B.: Rate enhancement in collisions of sulfuric acid molecules due to long-range intermolecular forces, Atmos. Chem. Phys., 19, 13355–13366, https://doi.org/10.5194/acp-19-13355-2019, 2019.

Haywood, J. and Boucher, O.: Estimates of the direct and indirect radiative forcing due to tropospheric aerosols: A review, Rev. Geophys., 38, 513–543, https://doi.org/10.1029/1999RG000078, 2000.

He, X.-C., Tham, Y. J., Dada, L., Wang, M., Finkenzeller, H., Stolzenburg, D., Iyer, S., Simon, M., Kürten, A., Shen, J., Rörup, B., Rissanen, M., Schobesberger, S., Baalbaki, R., Wang, D. S., Koenig, T. K., Jokinen, T., Sarnela, N., Beck, L. J., Almeida, J., Amanatidis, S., Amorim, A., Ataei, F., Baccarini, A., Bertozzi, B., Bianchi, F., Brilke, S., Caudillo, L., Chen, D., Chiu, R., Chu, B., Dias, A., Ding, A., Dommen, J., Duplissy, J., El Haddad, I., Gonzalez Carracedo, L., Granzin, M., Hansel, A., Heinritzi, M., Hofbauer, V., Junninen, H., Kangasluoma, J., Kemppainen, D., Kim, C., Kong, W., Krechmer, J. E., Kvashin, A., Laitinen, T., Lamkaddam, H., Lee, C. P., Lehtipalo, K., Leiminger, M., Li, Z., Makhmutov, V., Manninen, H. E., Marie, G., Marten, R., Mathot, S., Mauldin, R. L., Mentler, B., Möhler, O., Müller, T., Nie, W., Onnela, A., Petäjä, T., Pfeifer, J., Philippov, M., Ranjithkumar, A., Saiz-Lopez, A., Salma, I., Scholz, W., Schuchmann, S., Schulze, B., Steiner, G., Stozhkov, Y., Tauber, C., Tomé, A., Thakur, R. C., Väisänen, O., Vazquez-Pufleau, M., Wagner, A. C., Wang, Y., Weber, S. K., Winkler, P. M., Wu, Y., Xiao, M., Yan, C., Ye, Q., Ylisirniö, A., Zauner-Wieczorek, M., Zha, Q., Zhou, P., Flagan, R. C., Curtius, J., Baltensperger, U., Kulmala, M., Kerminen, V.-M., Kurtén, T., et al.: Role of iodine oxoacids in atmospheric aerosol nucleation, Science, 371, 589–595, https://doi.org/10.1126/science.abe0298, 2021.

He, X.-C., Simon, M., Iyer, S., Xie, H.-B., Rörup, B., Shen, J., Finkenzeller, H., Stolzenburg, D., Zhang, R., Baccarini, A., Tham, Y. J., Wang, M., Amanatidis, S., Piedehierro, A. A., Amorim, A., Baalbaki, R., Brasseur, Z., Caudillo, L., Chu, B., Dada, L., Duplissy, J., El Haddad, I., Flagan, R. C., Granzin, M., Hansel, A., Heinritzi, M., Hofbauer, V., Jokinen, T., Kemppainen, D., Kong, W., Krechmer, J., Kürten, A., Lamkaddam, H., Lopez, B., Ma, F., Mahfouz, N. G. A., Makhmutov, V., Manninen, H. E., Marie, G., Marten, R., Massabò, D., Mauldin, R. L., Mentler, B., Onnela, A., Petäjä, T., Pfeifer, J., Philippov, M., Ranjithkumar, A., Rissanen, M. P., Schobesberger, S., Scholz, W., Schulze, B., Surdu, M., Thakur, R. C., Tomé, A., Wagner, A. C., Wang, D., Wang, Y., Weber, S. K., Welti, A., Winkler, P. M., Zauner-Wieczorek, M., Baltensperger, U., Curtius, J., Kurtén, T., Worsnop, D. R., Volkamer, R., Lehtipalo, K., Kirkby, J., Donahue, N. M., Sipilä, M., and Kulmala, M.: Iodine oxoacids enhance nucleation of sulfuric acid particles in the atmosphere, Science, 382, 1308–1314, https://doi.org/10.1126/science.adh2526, 2023.

Heard, D. E., Read, K. A., Methven, J., Al-Haider, S., Bloss, W. J., Johnson, G. P., Pilling, M. J., Seakins, P. W., Smith, S. C., Sommariva, R., Stanton, J. C., Still, T. J., Ingham, T., Brooks, B., Leeuw, G. D., Jackson, A. V., McQuaid, J. B., Morgan, R., Smith, M. H., Carpenter, L. J., Carslaw, N., Hamilton, J., Hopkins, J. R., Lee, J. D., Lewis, A. C., Purvis, R. M., Wevill, D. J., Brough, N., Green, T., Mills, G., Penkett, S. A., Plane, J. M. C., Saiz-Lopez, A., Worton, D., Monks, P. S., Fleming, Z., Rickard, A. R., Alfarra, M. R., Allan, J. D., Bower, K., Coe, H., Cubison, M., Flynn, M., McFiggans, G., Gallagher, M., Norton,

E. G., O'Dowd, C. D., Shillito, J., Topping, D., Vaughan, G., Williams, P., Bitter, M., Ball, S. M., Jones, R. L., Povey, I. M., O'Doherty, S., Simmonds, P. G., Allen, A., Kinnersley, R. P., Beddows, D. C. S., Dall'Osto, M., Harrison, R. M., Donovan, R. J., Heal, M. R., Jennings, S. G., Noone, C., and Spain, G.: The North Atlantic Marine Boundary Layer Experiment (NAMBLEX). Overview of the campaign held at Mace Head, Ireland, in summer 2002, Atmos. Chem. Phys., 6, 2241–2272, https://doi.org/10.5194/acp-6-2241-2006, 2006.

Hirshorn, N. S., Zuromski, L. M., Rapp, C., McCubbin, I., Carrillo-Cardenas, G., Yu, F., and Hallar, A. G.: Seasonal significance of new particle formation impacts on cloud condensation nuclei at a mountaintop location, Atmos. Chem. Phys., 22, 15909–15924, https://doi.org/10.5194/acp-22-15909-2022, 2022.

Holzer, C., Franzke, Y. J., and Pausch, A.: Current density functional framework for spin–orbit coupling, J. Chem. Phys., 157, 204102, https://doi.org/10.1063/5.0122394, 2022.

Honrath, R. E., Lu, Y., Peterson, M. C., Dibb, J. E., Arsenault, M. A., Cullen, N. J., and Steffen, K.: Vertical fluxes of NO_x, HONO, and HNO_3 above the snowpack at Summit, Greenland, Atmos. Environ., 36, 2629–2640, https://doi.org/10.1016/S1352-2310(02)00132-2, 2002.

Humphrey, W., Dalke, A., and Schulten, K.: VMD: visual molecular dynamics, J. Mol. Graph., 14, 33–38, 1996.

Jones, A. E., Brough, N., Anderson, P. S., and Wolff, E. W.: HO_2NO_2 and HNO_3 in the coastal Antarctic winter night: a "lab-in-the-field" experiment, Atmos. Chem. Phys., 14, 11843–11851, https://doi.org/10.5194/acp-14-11843-2014, 2014.

Jurkat, T., Voigt, C., Kaufmann, S., Zahn, A., Sprenger, M., Hoor, P., Bozem, H., Müller, S., Dörnbrack, A., Schlager, H., Bönisch, H., and Engel, A.: A quantitative analysis of stratospheric HCl, HNO_3, and O_3 in the tropopause region near the subtropical jet, Geophys. Res. Lett., 41, 3315–3321, https://doi.org/10.1002/2013GL059159, 2014.

Khanniche, S., Louis, F., Cantrel, L., and Černušák, I.: A theoretical study of the microhydration of iodic acid ($HOIO_2$), Comput. Theor. Chem., 1094, 98–107, https://doi.org/10.1016/j.comptc.2016.09.010, 2016.

Khanniche, S., Louis, F., Cantrel, L., and Černušák, I.: Thermochemistry of HIO_2 Species and Reactivity of Iodous Acid with OH Radical: A Computational Study, ACS Earth Space Chem., 1, 39–49, https://doi.org/10.1021/acsearthspacechem.6b00010, 2017.

Koenig, T. K., Baidar, S., Campuzano-Jost, P., Cuevas, C. A., Dix, B., Fernandez, R. P., Guo, H., Hall, S. R., Kinnison, D., Nault, B. A., Ullmann, K., Jimenez, J. L., Saiz-Lopez, A., and Volkamer, R.: Quantitative detection of iodine in the stratosphere, Proc. Natl. Acad. Sci. U.S.A., 117, 1860–1866, https://doi.org/10.1073/pnas.1916828117, 2020.

Kubečka, J., Besel, V., Kurtén, T., Myllys, N., and Vehkamäki, H.: Configurational Sampling of Noncovalent (Atmospheric) Molecular Clusters: Sulfuric Acid and Guanidine, J. Phys. Chem. A, 123, 6022–6033, https://doi.org/10.1021/acs.jpca.9b03853, 2019.

Kühn, M. and Weigend, F.: Two-component hybrid time-dependent density functional theory within the Tamm-Dancoff approximation, J. Chem. Phys., 142, 034116, https://doi.org/10.1063/1.4905829, 2015.

Kulmala, M., Kontkanen, J., Junninen, H., Lehtipalo, K., Manninen, H. E., Nieminen, T., Petäjä, T., Sipilä, M., Schobesberger, S., Rantala, P., Franchin, A., Jokinen, T., Järvinen, E., Äijälä, M., Kangasluoma, J., Hakala, J., Aalto, P. P., Paasonen, P.,

Mikkilä, J., Vanhanen, J., Aalto, J., Hakola, H., Makkonen, U., Ruuskanen, T., Mauldin, R. L., Duplissy, J., Vehkamäki, H., Bäck, J., Kortelainen, A., Riipinen, I., Kurtén, T., Johnston, M. V., Smith, J. N., Ehn, M., Mentel, T. F., Lehtinen, K. E. J., Laaksonen, A., Kerminen, V.-M., and Worsnop, D. R.: Direct Observations of Atmospheric Aerosol Nucleation, Science, 339, 943–946, https://doi.org/10.1126/science.1227385, 2013.

Kurfman, L. A., Odbadrakh, T. T., and Shields, G. C.: Calculating Reliable Gibbs Free Energies for Formation of Gas-Phase Clusters that Are Critical for Atmospheric Chemistry: $(H_2SO_4)_3$, J. Phys. Chem. A, 125, 3169–3176, https://doi.org/10.1021/acs.jpca.1c00872, 2021.

Kürten, A., Ortega, I. K., Kupiainen-Määttä, O., Praplan, A. P., Adamov, A., Amorim, A., Bianchi, F., Breitenlechner, M., David, A., Dommen, J., Donahue, N. M., Downard, A., Dunne, E., Duplissy, J., Ehrhart, S., Flagan, R. C., Franchin, A., Guida, R., Hakala, J., Hansel, A., Heinritzi, M., Henschel, H., Jokinen, T., Junninen, H., Kajos, M., Kangasluoma, J., Keskinen, H., Kupc, A., Kurtén, T., Kvashin, A. N., Laaksonen, A., Lehtipalo, K., Leiminger, M., Leppä, J., Loukonen, V., Makhmutov, V., Mathot, S., McGrath, M. J., Nieminen, T., Olenius, T., Onnela, A., Petäjä, T., Riccobono, F., Riipinen, I., Rissanen, M., Rondo, L., Ruuskanen, T., Santos, F. D., Sarnela, N., Schallhart, S., Schnitzhofer, R., Seinfeld, J. H., Simon, M., Sipilä, M., Stozhkov, Y., Stratmann, F., Tomé, A., Tröstl, J., Tsagkogeorgas, G., Vaattovaara, P., Viisanen, Y., Virtanen, A., Vrtala, A., Wagner, P. E., Weingartner, E., Wex, H., Williamson, C., Wimmer, D., Ye, P., Yli-Juuti, T., Carslaw, K. S., Kulmala, M., Curtius, J., Baltensperger, U., Worsnop, D. R., Vehkamäki, H., and Kirkby, J.: Molecular understanding of sulphuric acid–amine particle nucleation in the atmosphere, Nature, 502, 359–363, https://doi.org/10.1038/nature12663, 2013.

Lane, J. R., Contreras-García, J., Piquemal, J.-P., Miller, B. J., and Kjaergaard, H. G.: Are Bond Critical Points Really Critical for Hydrogen Bonding?, J. Chem. Theory Comput., 9, 3263–3266, https://doi.org/10.1021/ct400420r, 2013.

Legrand, M., McConnell, J. R., Preunkert, S., Arienzo, M., Chellman, N., Gleason, K., Sherwen, T., Evans, M. J., and Carpenter, L. J.: Alpine ice evidence of a three-fold increase in atmospheric iodine deposition since 1950 in Europe due to increasing oceanic emissions, Proc. Natl. Acad. Sci. U.S.A., 115, 12136–12141, https://doi.org/10.1073/pnas.1809867115, 2018.

Lehtinen, K. E. J., Dal Maso, M., Kulmala, M., and Kerminen, V.-M.: Estimating nucleation rates from apparent particle formation rates and vice versa: Revised formulation of the Kerminen–Kulmala equation, J. Aerosol Sci., 38, 988–994, https://doi.org/10.1016/j.jaerosci.2007.06.009, 2007.

Lehtipalo, K., Rondo, L., Kontkanen, J., Schobesberger, S., Jokinen, T., Sarnela, N., Kürten, A., Ehrhart, S., Franchin, A., Nieminen, T., Riccobono, F., Sipilä, M., Yli-Juuti, T., Duplissy, J., Adamov, A., Ahlm, L., Almeida, J., Amorim, A., Bianchi, F., Breitenlechner, M., Dommen, J., Downard, A. J., Dunne, E. M., Flagan, R. C., Guida, R., Hakala, J., Hansel, A., Jud, W., Kangasluoma, J., Kerminen, V.-M., Keskinen, H., Kim, J., Kirkby, J., Kupc, A., Kupiainen-Määttä, O., Laaksonen, A., Lawler, M. J., Leiminger, M., Mathot, S., Olenius, T., Ortega, I. K., Onnela, A., Petäjä, T., Praplan, A., Rissanen, M. P., Ruuskanen, T., Santos, F. D., Schallhart, S., Schnitzhofer, R., Simon, M., Smith, J. N., Tröstl, J., Tsagkogeorgas, G., Tomé, A., Vaattovaara, P., Vehkamäki, H., Vrtala, A. E., Wagner, P. E., Williamson, C., Wimmer, D., Winkler, P. M., Virtanen, A., Donahue, N. M.,

Carslaw, K. S., Baltensperger, U., Riipinen, I., Curtius, J., Worsnop, D. R., and Kulmala, M.: The effect of acid–base clustering and ions on the growth of atmospheric nano-particles, Nat. Commun., 7, 11594, https://doi.org/10.1038/ncomms11594, 2016.

Lenthe, E. V., Baerends, E. J., and Snijders, J. G.: Relativistic regular two-component Hamiltonians, The Journal of Chemical Physics, 99, 4597–4610, https://doi.org/10.1063/1.466059, 1993.

Li, J., Carlson, B. E., Yung, Y. L., Lv, D., Hansen, J., Penner, J. E., Liao, H., Ramaswamy, V., Kahn, R. A., Zhang, P., Dubovik, O., Ding, A., Lacis, A. A., Zhang, L., and Dong, Y.: Scattering and absorbing aerosols in the climate system, Nat. Rev. Earth Environ., 3, 363–379, https://doi.org/10.1038/s43017-022-00296-7, 2022.

Li, J., Ning, A., Liu, L., and Zhang, X.: Atmospheric Bases-Enhanced Iodic Acid Nucleation: Altitude-Dependent Characteristics and Molecular Mechanisms, Environ. Sci. Technol., 58, 16962–16973, https://doi.org/10.1021/acs.est.4c06053, 2024a.

Li, J., Wu, N., Chu, B., Ning, A., and Zhang, X.: Molecular-level study on the role of methanesulfonic acid in iodine oxoacid nucleation, Atmos. Chem. Phys., 24, 3989–4000, https://doi.org/10.5194/acp-24-3989-2024, 2024b.

Liu, L., Li, H., Zhang, H., Zhong, J., Bai, Y., Ge, M., Li, Z., Chen, Y., and Zhang, X.: The role of nitric acid in atmospheric new particle formation, Phys. Chem. Chem. Phys., 20, 17406–17414, https://doi.org/10.1039/c8cp02719f, 2018.

Liu, L., Yu, F., Du, L., Yang, Z., Francisco, J. S., and Zhang, X.: Rapid sulfuric acid–dimethylamine nucleation enhanced by nitric acid in polluted regions, Proc. Natl. Acad. Sci. U.S.A., 118, e2108384118, https://doi.org/10.1073/pnas.2108384118, 2021.

Liu, L., Li, S., Zu, H., and Zhang, X.: Unexpectedly significant stabilizing mechanism of iodous acid on iodic acid nucleation under different atmospheric conditions, Sci. Total Environ., 859, 159832, https://doi.org/10.1016/j.scitotenv.2022.159832, 2023.

Lu, T. and Chen, F.: Multiwfn: A multifunctional wavefunction analyzer, J. Comput. Chem., 33, 580–592, https://doi.org/10.1002/jcc.22885, 2012.

Lu, T. and Chen, Q.: Shermo: A general code for calculating molecular thermochemistry properties, Comput. Theor. Chem., 1200, 113249, https://doi.org/10.1016/j.comptc.2021.113249, 2021.

Ma, F., Xie, H.-B., Zhang, R., Su, L., Jiang, Q., Tang, W., Chen, J., Engsvang, M., Elm, J., and He, X.-C.: Enhancement of Atmospheric Nucleation Precursors on Iodic Acid-Induced Nucleation: Predictive Model and Mechanism, Environ. Sci. Technol., 57, 6944–6954, https://doi.org/10.1021/acs.est.3c01034, 2023.

McGrath, M. J., Olenius, T., Ortega, I. K., Loukonen, V., Paasonen, P., Kurtén, T., Kulmala, M., and Vehkamäki, H.: Atmospheric Cluster Dynamics Code: a flexible method for solution of the birth-death equations, Atmos. Chem. Phys., 12, 2345–2355, https://doi.org/10.5194/acp-12-2345-2012, 2012.

Mehra, M., Wang, Y., Ramesh, C. B., Zhang, R., Zhang, J., Giangrande, S. E., and Wang, J.: Deep Convection-Driven Downward Transport of Trace Gases and Aerosols From the Free Troposphere to the Boundary Layer, Geophys. Res. Lett., 53, e2025GL119490, https://doi.org/10.1029/2025GL119490, 2026.

Neese, F.: The ORCA program system, WIREs Comput. Mol. Sci., 2, 73–78, https://doi.org/10.1002/wcms.81, 2012.

Ning, A., Liu, L., Zhang, S., Yu, F., Du, L., Ge, M., and Zhang, X.: The critical role of dimethylamine in the rapid formation of iodic acid particles in marine areas, npj Clim Atmos Sci, 5, 92, https://doi.org/10.1038/s41612-022-00316-9, 2022.

Olenius, T., Kupiainen-Määttä, O., Ortega, I. K., Kurtén, T., and Vehkamäki, H.: Free energy barrier in the growth of sulfuric acid–ammonia and sulfuric acid–dimethylamine clusters, J. Chem. Phys., 139, 084312, https://doi.org/10.1063/1.4819024, 2013.

Peterson, K. A., Figgen, D., Goll, E., Stoll, H., and Dolg, M.: Systematically convergent basis sets with relativistic pseudopotentials. II. Small-core pseudopotentials and correlation consistent basis sets for the post-d group 16–18 elements, J. Chem. Phys., 119, 11113–11123, https://doi.org/10.1063/1.1622924, 2003.

Pope, C. A. and Dockery, D. W.: Health Effects of Fine Particulate Air Pollution: Lines that Connect, J. Air Waste Manage. Assoc., 56, 709–742, https://doi.org/10.1080/10473289.2006.10464485, 2006.

Qi, X., Li, Z., Zhao, C., Zhang, Q., and Zhou, Y.: Environmental impacts of Arctic shipping activities: A review, Ocean Coast. Manag., 247, 106936, https://doi.org/10.1016/j.ocecoaman.2023.106936, 2024.

Randel, W. J., Park, M., Emmons, L., Kinnison, D., Bernath, P., Walker, K. A., Boone, C., and Pumphrey, H.: Asian Monsoon Transport of Pollution to the Stratosphere, Science, 328, 611–613, https://doi.org/10.1126/science.1182274, 2010.

Ranjithkumar, A., Gordon, H., Williamson, C., Rollins, A., Pringle, K., Kupc, A., Abraham, N. L., Brock, C., and Carslaw, K.: Constraints on global aerosol number concentration, SO_2 and condensation sink in UKESM1 using ATom measurements, Atmos. Chem. Phys., 21, 4979–5014, https://doi.org/10.5194/acp-21-4979-2021, 2021.

Rappe, A. K., Casewit, C. J., Colwell, K. S., Goddard, W. A., and Skiff, W. M.: UFF, a full periodic table force field for molecular mechanics and molecular dynamics simulations, J. Am. Chem. Soc., 114, 10024–10035, https://doi.org/10.1021/ja00051a040, 1992.

Rolfes, J. D., Neese, F., and Pantazis, D. A.: All-electron scalar relativistic basis sets for the elements Rb–Xe, J. Comput. Chem., 41, 1842–1849, https://doi.org/10.1002/jcc.26355, 2020.

Salignat, R., Rissanen, M., Iyer, S., Baray, J.-L., Tulet, P., Metzger, J.-M., Brioude, J., Sellegri, K., and Rose, C.: Measurement report: Insights into the chemical composition and origin of molecular clusters and potential precursor molecules present in the free troposphere over the southern Indian Ocean: observations from the Maïdo Observatory (2150 m a.s.l., Réunion), Atmos. Chem. Phys., 24, 3785–3812, https://doi.org/10.5194/acp-24-3785-2024, 2024.

Sarr, S., Graton, J., Rahali, S., Montavon, G., and Galland, N.: Delocalized relativistic effects, from the viewpoint of halogen bonding, Phys. Chem. Chem. Phys., 23, 4064–4074, https://doi.org/10.1039/D0CP05840H, 2021.

Schmitz, G. and Elm, J.: Assessment of the DLPNO Binding Energies of Strongly Noncovalent Bonded Atmospheric Molecular Clusters, ACS Omega, 5, 7601–7612, https://doi.org/10.1021/acsomega.0c00436, 2020.

Shen, J., Russell, D. M., DeVivo, J., Kunkler, F., Baalbaki, R., Mentler, B., Scholz, W., Yu, W., Caudillo-Plath, L., Sommer, E., Ahongshangbam, E., Alfaouri, D., Almeida, J., Amorim, A., Beck, L. J., Beckmann, H., Berntheusel, M., Bhattacharyya, N., Canagaratna, M. R., Chassaing, A., Cruz-Simbron, R., Dada, L., Duplissy, J., Gordon, H., Granzin, M., Große Schute, L., Heinritzi, M., Iyer, S., Klebach, H., Krüger, T., Kürten, A., Lampimäki, M., Liu, L., Lopez, B., Martinez, M., Morawiec, A.,

Onnela, A., Peltola, M., Rato, P., Reza, M., Richter, S., Rörup, B., Sebastian, M. K., Simon, M., Surdu, M., Tamme, K., Thakur, R. C., Tomé, A., Tong, Y., Top, J., Umo, N. S., Unfer, G., Vettikkat, L., Weissbacher, J., Xenofontos, C., Yang, B., Zauner-Wieczorek, M., Zhang, J., Zheng, Z., Baltensperger, U., Christoudias, T., Flagan, R. C., El Haddad, I., Junninen, H., Möhler, O., Riipinen, I., Rohner, U., Schobesberger, S., Volkamer, R., Winkler, P. M., Hansel, A., Lehtipalo, K., Donahue, N. M., Lelieveld, J., Harder, H., Kulmala, M., Worsnop, D. R., Kirkby, J., Curtius, J., and He, X.-C.: New particle formation from isoprene under upper-tropospheric conditions, Nature, 636, 115–123, https://doi.org/10.1038/s41586-024-08196-0, 2024.

Sipilä, M., Sarnela, N., Jokinen, T., Henschel, H., Junninen, H., Kontkanen, J., Richters, S., Kangasluoma, J., Franchin, A., Peräkylä, O., Rissanen, M. P., Ehn, M., Vehkamäki, H., Kurten, T., Berndt, T., Petäjä, T., Worsnop, D., Ceburnis, D., Kerminen, V.-M., Kulmala, M., and O'Dowd, C.: Molecular-scale evidence of aerosol particle formation via sequential addition of HIO_3, Nature, 537, 532–534, https://doi.org/10.1038/nature19314, 2016.

Stewart, J. J. P.: Optimization of parameters for semiempirical methods VI: more modifications to the NDDO approximations and re-optimization of parameters, J. Mol. Model., 19, 1–32, https://doi.org/10.1007/s00894-012-1667-x, 2013.

Stewart, J. J. P.: MOPAC2016; Colorado Springs; CO (USA), http://openmopac.net/MOPAC2016.html (last access: 22 Feb 2024), 2016.

Tost, H.: Chemistry–climate interactions of aerosol nitrate from lightning, Atmos. Chem. Phys., 17, 1125–1142, https://doi.org/10.5194/acp-17-1125-2017, 2017.

Twohy, C. H., Clement, C. F., Gandrud, B. W., Weinheimer, A. J., Campos, T. L., Baumgardner, D., Brune, W. H., Faloona, I., Sachse, G. W., Vay, S. A., and Tan, D.: Deep convection as a source of new particles in the midlatitude upper troposphere, J. Geophys. Res., 107, https://doi.org/10.1029/2001JD000323, 2002.

Wang, J., Krejci, R., Giangrande, S., Kuang, C., Barbosa, H. M. J., Brito, J., Carbone, S., Chi, X., Comstock, J., Ditas, F., Lavric, J., Manninen, H. E., Mei, F., Moran-Zuloaga, D., Pöhlker, C., Pöhlker, M. L., Saturno, J., Schmid, B., Souza, R. A. F., Springston, S. R., Tomlinson, J. M., Toto, T., Walter, D., Wimmer, D., Smith, J. N., Kulmala, M., Machado, L. A. T., Artaxo, P., Andreae, M. O., Petäjä, T., and Martin, S. T.: Amazon boundary layer aerosol concentration sustained by vertical transport during rainfall, Nature, 539, 416–419, https://doi.org/10.1038/nature19819, 2016.

Wang, M., Xiao, M., Bertozzi, B., Marie, G., Rörup, B., Schulze, B., Bardakov, R., He, X.-C., Shen, J., Scholz, W., Marten, R., Dada, L., Baalbaki, R., Lopez, B., Lamkaddam, H., Manninen, H. E., Amorim, A., Ataei, F., Bogert, P., Brasseur, Z., Caudillo, L., De Menezes, L.-P., Duplissy, J., Ekman, A. M. L., Finkenzeller, H., Carracedo, L. G., Granzin, M., Guida, R., Heinritzi, M., Hofbauer, V., Höhler, K., Korhonen, K., Krechmer, J. E., Kürten, A., Lehtipalo, K., Mahfouz, N. G. A., Makhmutov, V., Massabò, D., Mathot, S., Mauldin, R. L., Mentler, B., Müller, T., Onnela, A., Petäjä, T., Philippov, M., Piedehierro, A. A., Pozzer, A., Ranjithkumar, A., Schervish, M., Schobesberger, S., Simon, M., Stozhkov, Y., Tomé, A., Umo, N. S., Vogel, F., Wagner, R., Wang, D. S., Weber, S. K., Welti, A., Wu, Y., Zauner-Wieczorek, M., Sipilä, M., Winkler, P. M., Hansel, A., Baltensperger, U., Kulmala, M., Flagan, R. C., Curtius, J., Riipinen, I., Gordon, H., Lelieveld, J., El-Haddad, I., Volkamer, R., Worsnop, D. R., Christoudias, T., Kirkby, J., Möhler, O., and Donahue, N. M.: Synergistic HNO_3–H_2SO_4–NH_3 upper tropospheric particle formation, Nature, 605, 483–489, https://doi.org/10.1038/s41586-022-04605-4, 2022.

Wang, Y., Fu, X., Wu, D., Wang, M., Lu, K., Mu, Y., Liu, Z., Zhang, Y., and Wang, T.: Agricultural Fertilization Aggravates Air Pollution by Stimulating Soil Nitrous Acid Emissions at High Soil Moisture, Environ. Sci. Technol., 55, 14556–14566, https://doi.org/10.1021/acs.est.1c04134, 2021.

Williamson, C. J., Kupc, A., Axisa, D., Bilsback, K. R., Bui, T., Campuzano-Jost, P., Dollner, M., Froyd, K. D., Hodshire, A. L., Jimenez, J. L., Kodros, J. K., Luo, G., Murphy, D. M., Nault, B. A., Ray, E. A., Weinzierl, B., Wilson, J. C., Yu, F., Yu, P., Pierce, J. R., and Brock, C. A.: A large source of cloud condensation nuclei from new particle formation in the tropics, Nature, 574, 399–403, https://doi.org/10.1038/s41586-019-1638-9, 2019.

Xiao, Q., Zhang, J., Wang, Y., Ziemba, L. D., Crosbie, E., Winstead, E. L., Robinson, C. E., DiGangi, J. P., Diskin, G. S., Reid, J. S., Schmidt, K. S., Sorooshian, A., Hilario, M. R. A., Woods, S., Lawson, P., Stamnes, S. A., and Wang, J.: New particle formation in the tropical free troposphere during CAMP^2 Ex: statistics and impact of emission sources, convective activity, and synoptic conditions, Atmos. Chem. Phys., 23, 9853–9871, https://doi.org/10.5194/acp-23-9853-2023, 2023.

Xu, W., Liu, L., Cheng, M., Zhao, Y., Zhang, L., Pan, Y., Zhang, X., Gu, B., Li, Y., Zhang, X., Shen, J., Lu, L., Luo, X., Zhao, Y., Feng, Z., Collett Jr., J. L., Zhang, F., and Liu, X.: Spatial–temporal patterns of inorganic nitrogen air concentrations and deposition in eastern China, Atmos. Chem. Phys., 18, 10931–10954, https://doi.org/10.5194/acp-18-10931-2018, 2018.

Yu, H., Ren, L., Huang, X., Xie, M., He, J., and Xiao, H.: Iodine speciation and size distribution in ambient aerosols at a coastal new particle formation hotspot in China, Atmos. Chem. Phys., 19, 4025–4039, https://doi.org/10.5194/acp-19-4025-2019, 2019.

Zhang, J. and Dolg, M.: ABCluster: the artificial bee colony algorithm for cluster global optimization, Phys. Chem. Chem. Phys., 17, 24173–24181, https://doi.org/10.1039/C5CP04060D, 2015.

Zhang, R.: Getting to the Critical Nucleus of Aerosol Formation, Science, 328, 1366–1367, https://doi.org/10.1126/science.1189732, 2010.

Zhang, R., Khalizov, A., Wang, L., Hu, M., and Xu, W.: Nucleation and Growth of Nanoparticles in the Atmosphere, Chem. Rev., 112, 1957–2011, https://doi.org/10.1021/cr2001756, 2012.

Zhang, R., Ma, F., Zhang, Y., Chen, J., Elm, J., He, X.-C., and Xie, H.-B.: HIO_3–HIO_2-Driven Three-Component Nucleation: Screening Model and Cluster Formation Mechanism, Environ. Sci. Technol., 58, 649–659, https://doi.org/10.1021/acs.est.3c06098, 2023.

Zu, H., Zhang, S., Liu, L., and Zhang, X.: The vital role of sulfuric acid in iodine oxoacids nucleation: impacts of urban pollutants on marine atmosphere, Environ. Res. Lett., https://doi.org/10.1088/1748-9326/ad193f, 2023.

Zu, H., Chu, B., Lu, Y., Liu, L., and Zhang, X.: Rapid iodine oxoacid nucleation enhanced by dimethylamine in broad marine regions, Atmos. Chem. Phys., 24, 5823–5835, https://doi.org/10.5194/acp-24-5823-2024, 2024.